

Lee, M.R., Tomkinson, T., Mark, D.F., Stuart, F.M., and Smith, C.L. (2013) *Evidence for silicate dissolution on Mars from the Nakhla meteorite*. *Meteoritics and Planetary Science*, 48 (2). pp. 224-240. ISSN 1086-9379

Copyright © 2012 The Meteoritical Society

<http://eprints.gla.ac.uk/74796/>

Deposited on: 31 January 2013

Evidence for silicate dissolution on Mars from the Nakhla meteorite

M.R. Lee^{1*}, T. Tomkinson², D.F. Mark², F.M. Stuart² and C.L. Smith^{3,4,5}

¹School of Geographical and Earth Sciences, University of Glasgow, Gregory Building, Lilybank Gardens, Glasgow G12 8QQ, U.K. ²Scottish Universities Environmental Research Centre, Rankine Avenue, Scottish Enterprise Technology Park, East Kilbride, G75 0QF, U.K. ³Department of Mineralogy, Natural History Museum (London), Cromwell Road, London SW7 5BD, U.K.

⁴European Space Agency ESTEC, Keplerlaan 1, 2200 AG Noordwijk, The Netherlands. ⁵UK Space Agency, ESA Harwell Centre, Atlas Building, Harwell Oxford, Didcot, Oxfordshire, OX11 0QX, U.K.

*Corresponding author. E-mail: Martin.Lee@glasgow.ac.uk

Abstract-Veins containing carbonates, hydrous silicates and sulphates that occur within and between grains of augite and olivine in the Nakhla meteorite are good evidence for the former presence of liquid water in the Martian crust. Aqueous solutions gained access to grain interiors *via* narrow fractures, and those fractures within olivine whose walls were oriented close to (001) were preferentially widened by etching along [001]. This orientation selective dissolution may have been due to the presence within olivine of shock-formed [001](100) and [001]{110} screw dislocations. The duration of etching is likely to have been brief, possibly less than a year, and the solutions responsible were sufficiently cool and reducing that laihunite is absent and Fe liberated from the olivine was not immediately oxidised. The pores within olivine were mineralised in sequence by siderite, nanocrystalline smectite, a Fe-Mg phyllosilicate, and then gypsum, whereas only the smectite occurs within augite. The nanocrystalline smectite was deposited as sub-micrometre thick layers on etched vein walls, and solution compositions varied substantially between and sometimes during precipitation of each layer. Together with microcrystalline gypsum the Fe-Mg phyllosilicate crystallised as water briefly returned to some of the veins following desiccation fracturing of the smectite. These results show that etching of olivine enhanced the porosity and permeability of the nakhlite parent rock and that dissolution and secondary mineralization took place within the same near-static aqueous system.

INTRODUCTION

The nakhlite meteorites are samples of the Martian crust and formed ~1400 Ma ago either within a lava flow or a shallow sill (Friedman-Lentz et al., 1999; Treiman, 2005; Korochantseva et al., 2011). They are clinopyroxenites, mostly olivine-bearing, and are inferred to have crystallised at different depths within the igneous body. Their relative positions within the flow or sill have been estimated from cooling rates inferred using olivine zoning (Mikouchi et al., 2003; 2006; 2012), from carbonate $\delta^{13}\text{C}$ values (Grady et al., 2007) and secondary mineralogy (Bridges and Warren, 2006; Changela and Bridges, 2011). However it is also possible that the nakhlite parent rock was sourced from more than one magma reservoir (Shirai and Ebihara, 2008) and contains multiple flows (Lentz et al. 2005), thus complicating attempts to fit all of the meteorites into a single genetic series.

Despite their magmatic origin, the nakhlites provide a unique insight into the nature of the Martian hydrosphere because they contain hydrous silicates, carbonates, iron oxide/oxyhydroxides and sulphate and chloride evaporites that formed from liquid water (e.g. Ashworth and Hutchison, 1975; Gooding et al., 1991; Treiman et al., 1993; Bridges and Grady, 2000; Needham et al., 2011). These secondary minerals are most prominent within veins that cross-cut olivine, but they also occur in the mesostasis and more rarely within augite grains (Treiman 2005). The weighted average of K-Ar and Rb-Sr age determinations of secondary minerals in the nakhlites Lafayette and Yamato [Y]-000593 is 633 ± 23 Ma (Borg and Drake, 2005 and references therein), and so the differences between ages of host rock crystallisation and secondary mineralisation mean that the aqueous solutions cannot have been linked to the magmatism. Instead they may have been sourced from the planet's surface (Bridges et al., 2001; Rao et al., 2005) or by the melting of crustal ices (Sawyer et al., 2000). In the most recent and comprehensive model, Changela and Bridges (2011) suggest that the secondary minerals formed within a very short-lived (< 1 yr) hydrothermal system that developed following melting of subsurface ices upon impact heating of the nakhlite parent rock. They also proposed that the secondary minerals were deposited within shock-formed fractures as the hydrothermal system cooled, and that heat loss was sufficiently rapid that one of the main constituents of the secondary mineral assemblage, a hydrous Fe-Mg silicate, had insufficient time to crystallise and so has remained as an amorphous silicate 'gel'.

Two important implications for our understanding of the hydrosphere of Mars that follow from the Changela and Bridges (2011) model are that: (i) during the Amazonian water may have been present only transiently in the Martian crust, and (ii) the establishment of a spatially extensive aqueous system at this relatively late-stage in the planet's history required a source of heat to melt subsurface ices together with substantial shock pressure to fracture the rock and so render it sufficiently porous and permeable to enable fluid ingress and flow. Here we have sought to understand better the spatial scale and dynamics of the aqueous system by testing the Changela and Bridges model, and specifically by asking: (i) was shock necessary to enable aqueous solutions access to the nakhlite parent rock? and (ii) were all of the ions needed for the secondary minerals imported from elsewhere in the crust *via* an extensive aqueous system (i.e., allochemical), or were solutes sourced intraformationally by interaction of water with nakhlite olivine and mesostasis glass, as suggested by Treiman (1993) and Treiman and Lindstrom (1997) (i.e. near-isochemical)? This second question is also relevant to the problem of why the secondary minerals are much more abundant within olivine than the volumetrically dominant augite.

These questions have been addressed by studying veins of secondary minerals in freshly prepared samples of the Nakhla meteorite using electron beam imaging, diffraction and

microanalysis. One focus of this work has been to determine how the abundance and width of veins relates to their crystallographic orientation within olivine. Such measurements have not been undertaken previously on the nakhlites, but have been highly instructive about the nature of fluid-rock interactions in terrestrial olivine-rich rocks (e.g. Banfield et al., 1990; Boudier et al., 2010; Plümper et al., 2012). We have also examined the rough surfaces of olivine grains that have been freshly broken from the meteorite in order to obtain a new perspective on the microstructure of the veins and their secondary minerals. This study has used Nakhla because it is the only fall among the nakhlites and so will have undergone the minimum of terrestrial alteration. By contrast the nakhlite finds contain evidence for terrestrial dissolution of primary (magmatic) minerals, dissolution and/or recrystallisation of secondary minerals, and even crystallisation of new minerals (e.g. Velbel, 2008; Noguchi et al., 2009; Hallis and Taylor, 2011), which all can significantly complicate any attempt to understand Martian aqueous processes.

MATERIALS AND METHODS

Nakhla is an olivine clinopyroxenite that contains ~90 % augite. The augite is zoned from a $\text{Wo}_{39}\text{En}_{38}\text{Fs}_{23}$ core to a $\text{Wo}_{38}\text{En}_{25}\text{Fs}_{37}$ rim (Mikouchi et al., 2000). Olivine grains are coarser, zoned from $\text{Fa}_{68}\text{-Fa}_{60}$, and contain up to 0.5 wt% CaO (Harvey and McSween, 1992; Mikouchi et al., 2000). The olivine also hosts augite-magnetite symplectites that were formed by exsolution at >900 °C and under oxidising conditions (Mikouchi et al., 2000). Secondary minerals within Nakhla comprise goethite, a hydrous Fe-Mg silicate variously referred to as ‘rust’, smectite, or ‘gel’, carbonates ($\text{Cc}_{0.4-4.2}\text{Mg}_{16.9-29.4}\text{Sd}_{45.4-64.7}\text{Rd}_{37.2-1.7}$) hereafter referred to as siderite, Ca- and Mg-sulphates, and halite (Gooding et al., 1991; Bridges and Grady, 2000; Changela and Bridges, 2011; Needham et al., 2011). The carbonates and silicates form ~6 µm wide veins that occupy ~3 vol. % of the olivine grains, and also occur less abundantly within augite and the mesostasis (Changela and Bridges, 2011).

Nakhla was ejected from Mars at 10.8 ± 0.8 Ma (Eugster et al., 2002) and was seen to fall in Egypt in 1911, although the sample studied here was recovered two years later. The olivine grains examined originate from 1.7g chip that was separated from a bulk sample, BM1913, 25, held by the Natural History Museum (London). This chip was taken from the interior of the bulk sample and approximately 5 cm from the fusion crust in order to minimise any potential contamination from a century of terrestrial residence. Most of the results reported here are from rough and freshly exposed surfaces of sub-millimetre sized olivine grains that had broken from the chip during its separation from BM1913, 25. These ‘olivine grain fragments’ were collected using tweezers and placed on adhesive C tabs for study. Larger (millimetre-sized) pieces containing both olivine and augite were also made into polished thin sections after impregnation in resin, and immediately prior to electron backscatter diffraction (EBSD) work they were repolished for ~5 minutes in colloidal silica.

The olivine grain fragments and polished samples were examined using two field-emission scanning electron microscopes (SEMs). The FEI Quanta is equipped with an EDAX Genesis integrated energy-dispersive X-ray spectrometer (EDX) and EBSD system whereas the Zeiss Sigma is equipped with an Oxford Instruments-HKL integrated EDX-EBSD system. Owing to their small size the olivine grain fragments did not charge appreciably during electron irradiation and so secondary electron (SE) and backscattered electron (BSE) images could be obtained from them at high vacuum and without the need for prior Au or C coating. The SE images were acquired at 5 kV and BSE images at 20 kV. X-ray maps were obtained from the uncoated grain fragments using an

Oxford Instruments 80 mm silicon-drift X-ray detector attached to the Zeiss SEM and operated through INCA software. These maps were collected at 20 kV and using a 1024×768 pixel resolution. As they are ‘spectrum maps’ X-ray spectra can be extracted from any pixel or group of pixels by post-processing. BSE images of uncoated polished samples were acquired at 20 kV/1-2 nA and with the SEM operated in a low vacuum (~50 Pa) mode.

The chemical compositions of minerals in thin section were quantified by electron probe microanalysis (EPMA) using a Cameca SX100 in the School of Geosciences, University of Edinburgh. The instrument was operated at 15 kV for all analyses. Calibration used jadeite (Na), spinel (Mg, Al), wollastonite (Si, Ca), apatite (P), barite (S), halite (Cl), orthoclase (K), rutile (Ti), Cr metal (Cr), Mn metal (Mn), fayalite (Fe) and Ni metal (Ni). Chemical compositions of olivine and pyroxene were measured using a ~1 µm diameter beam at currents of 10 nA (Na, Mg, Si and Fe) and 100 nA (Al, K, Ca, Ti, Cr, Mn and Ni). Peak/background counting times were 20/10 to 40/20 seconds, depending on the element being analysed. Typical elemental detection limits, in wt%, for each oxide are as follows: Na₂O (0.04), MgO (0.03), Al₂O₃ (0.06), SiO₂ (0.13), K₂O (0.01), CaO (0.07), TiO₂ (0.01), Cr₂O₃ (0.02), MnO (0.09), FeO (0.11), NiO (0.03). The compositions of vein-filling Fe-Mg silicates were determined using a ~2 µm diameter defocused beam at currents of 1 nA (Na, Mg, Al, Si, Ca and Fe) and 80 nA (P, S, Cl, K, Ti, Cr, Mn and Ni). Typical elemental detection limits, in wt%, are as follows: Na₂O (0.18), MgO (0.13), Al₂O₃ (0.28), SiO₂ (0.49), P₂O₅ (0.02), SO₃ (0.02), Cl (0.01), K₂O (0.01), CaO (0.15), TiO₂ (0.02), Cr₂O₃ (0.02), MnO (0.08), FeO (0.56), NiO (0.03).

The crystallographic orientation of olivine grains in the polished sections was determined using the EDAX-TSL EBSD system. EBSD mapping was undertaken on uncoated thin sections under low vacuum (~50-70 Pa), at 20 kV and a relatively high beam current (not quantified by the Quanta SEM). Kikuchi patterns were acquired at a rate of ~20 patterns sec⁻¹ and a step size of ~0.3 µm. The patterns were indexed using the structure file for olivine in the TSL database, and the orientations of the poles to various lattice planes in the mapped samples are plotted on upper hemisphere stereographic pole figures. These pole figures reveal the orientations of lattice planes relative to the thin section surface. However EBSD does not enable determination of the true orientation of a feature seen in thin section, for example a fracture, unless the inclination of the fracture relative to the polished surface is also known so it can be compared with the inclinations of various lattice planes. Thus where a feature is oriented parallel to the line made by the intersection of a lattice plane with the thin section surface but its three-dimensional orientation is unknown, the feature is described as being parallel to the ‘trace’ of that lattice plane.

For transmission electron microscope (TEM) work electron-transparent foils were cut from the surfaces of Au coated olivine grain fragments and C coated polished thin sections. The foils were prepared using a FEI Duomill dual-beam focused ion beam (FIB) instrument operated with a 30 kV Ga⁺ ion beam and following the procedure of Lee et al. (2003). Prior to starting milling the area of interest was capped with a 15 µm long by 4 µm wide and 0.1 µm thick layer of Pt that was applied using a gas injection system and deposited by interaction with the electron beam. Initially each foil was ion milled to a thickness of ~2 µm using high (~1 nA) beam currents. Following its *in-situ* extraction the thick foil was welded to the tines of a copper holder using electron and ion beam-deposited Pt and reduced to ~90 nm thickness at lower current (~100 pA). Trenches were also cut into the thin section surface so that the 3D orientation of veins and fractures could be determined. These trenches were milled to a depth of ~3 µm over a 5.5 µm × 22 µm area and using the same conditions as for foil preparation. The foils were imaged initially by low voltage scanning

transmission electron microscopy (LV-STEM) using a STEM detector on the Zeiss SEM. The SEM was operated at 20 kV/1 nA and the detector enables acquisition of both bright-field and annular dark-field images (see Lee and Smith, 2006). Bright-field diffraction-contrast images, high-resolution images and selected area electron diffraction (SAED) patterns were acquired from the foils using a FEI T20 TEM operated at 200 kV. The true crystallographic orientations of olivine microstructures were determined by acquiring TEM image/SAED pattern pairs at several different values of rotate and tilt of the double-tilt goniometer holder and plotting their traces on a stereogram.

RESULTS

Secondary mineral veins in thin section

EPMA yields compositions for augite and olivine of $\text{Wo}_{38}\text{En}_{37}\text{Fs}_{26}$ ($n=4$) and $\text{Fa}_{66.8}$ ($n=7$) respectively (Table 1), which are consistent with previous analyses of Nakhla silicates. Secondary mineral veins up to 5 μm in width cross-cut augite and olivine grains and lie along their mutual boundaries (Figs. 1–4). The widest veins within olivine may traverse entire grains or terminate within them, and EBSD shows that they are oriented parallel or at a shallow angle to $(001)_{\text{ol}}$ (Figs. 1 and 3). Very narrow veins cross-cut olivine parallel to the trace of $(010)_{\text{ol}}$, and hairline fractures extend parallel to the trace of $(001)_{\text{ol}}$ from intragranular boundaries and vein walls (Fig. 1). Intergranular veins are widest where the olivine vein wall lies close to $(001)_{\text{ol}}$ and they ‘pinch out’ as it changes orientation, for example towards the trace of $(010)_{\text{ol}}$ (Fig. 2). The olivine walls of (001) parallel intragranular veins are very finely serrated, and the teeth and notches are elongate along $[001]_{\text{ol}}$ (Figs. 2 and 3a). A foil was cut from the vein in Figure 3a and SAED shows that olivine on either side differs in orientation by $\sim 5^\circ$, thus demonstrating that this vein has formed along a low angle subgrain boundary. The olivine contains dislocations at a density of $\sim 2 \times 10^8 \text{ cm}^{-2}$ that lie in the (100) plane and are parallel to $[001]$ (Fig. 3b). The secondary mineral veins within augite grains are very narrow and their walls may be straight or very finely serrated, termed ‘microdenticulate’ by Velbel (2012) (Fig. 2).

All of the inter- and intra-granular veins contain a Fe-Mg silicate that is compositionally very similar to secondary minerals previously found in Nakhla and described as ‘rust’ (“probably smectite”) by Gooding et al. (1991) and a ‘gel’ by Changela and Bridges (2011) (Table 2). The low analytical totals of this Fe-Mg silicate demonstrate that it is hydrous, and in the FIB produced foils it yields SAED patterns with continuous rings indicating that it is very finely crystalline (Fig. 3d). Throughout most of the vein in Figure 3 the Fe-Mg silicate is compact, but where it is in direct contact with olivine at the base of the vein it is more open textured and contains circular crystallites (Fig. 3d). This fine-scale interpenetration of Fe-Mg silicate with olivine (Fig. 3c) suggests a replacive origin. Fe-Mg silicate is the only observed constituent of veins in augite (Fig. 2), whereas it is often accompanied by Fe-Mg-Mn-Ca siderite within olivine (Figs. 1–3), and the carbonate usually lines both vein walls (Figs. 3a–c). Where veins have developed between augite and olivine, the siderite occurs only on the olivine wall (Fig. 2).

Augite-magnetite symplectites occur along augite-olivine grain boundaries and within olivine grains. The intergranular symplectites in Figures 1 and 2 are in contact with augite but otherwise enclosed by secondary minerals. Intragranular symplectites are 20–30 μm long by $<1 \mu\text{m}$ wide lamellae that lie parallel to the trace of $(100)_{\text{ol}}$ (Fig. 4), and Mikouchi et al. (2000) showed that $(100)_{\text{ol}}$ is their true orientation. These lamellae cross-cut Fe-Mg silicate veins oriented close to $(010)_{\text{ol}}$, albeit with some distortion, but are cut and slightly offset by open fractures in the same

orientation (Fig. 4). Lath-shaped crystals of augite $\sim 30\ \mu\text{m}$ long by $\sim 2\ \mu\text{m}$ wide also occur as inclusions within the olivine grains. Their long and short axes are parallel to the traces of $(010)_{\text{ol}}$ and $(001)_{\text{ol}}$ respectively. The augite of some of these inclusions is intergrown with a Fe- and O-bearing mineral that yielded backscatter Kikuchi patterns that index as magnetite, but from these observations alone it is unknown whether the augite-magnetite laths are a previously undescribed variety of symplectite.

Olivine grain fragments

Twenty sub-millimetre sized olivine grain fragments were studied by SEM, and their surfaces may be featureless (apart for irregular steps), covered in regularly spaced pits, or they can possess a continuous or patchy Fe-Mg silicate coating. Four of the grain fragments have pitted surfaces and the pits are oval to sub-circular in profile, ~ 0.8 to $10\ \mu\text{m}$ in diameter, and have faceted walls that lie at low angles to the grain surface (Figs. 5 and 6a-c). These pits typically occur together in parallel lines and all pits in each line are the same size and shape, although pits in adjacent lines may differ significantly in their diameter and depth (Fig. 6a). A foil was extracted from the grain fragment in Figure 5 using the FIB technique and the crystallographic orientation of olivine in this foil indicates that the pitted grain surfaces lie close to (100) and (010) .

The grain coatings are patchy and have broken to expose multiple layers that range from sub-micrometre to a few micrometres in thickness (Figs 5, 6b and 6c). The thinnest layers line olivine grain surfaces including the walls and floors of the pits, and their outer surfaces have a nanoscale ornamentation (Fig. 6c). Thicker parts of the coatings either have a very smooth and featureless outer surface or are covered in micrometre-sized ‘humps’ whose walls are planar and angled outwards and whose tops are domed or flat (Fig. 6a, b). These humps occur together in lines that are oriented parallel to lines of pits in the underlying olivine, and they are similar in size and shape to the olivine pits (Fig. 6b). TEM images of a foil that was cut through a hump shows that there is a pit in the olivine beneath whose profile is a mirror image of the hump above (Fig. 6d). The walls of this pit are planar and their crystallographic orientations are shown in Figure 6d. The hump and its underlying pit are occupied entirely by a Fe-Mg silicate coating that is finely crystalline and yields SAED patterns with continuous rings whose d-spacings are 0.256 and 0.157 nm (Fig. 6d). Lattice fringe images were however unobtainable owing to the thickness of the foil. Olivine immediately beneath the pit contains linear defects and SAED trace analysis shows that they lie parallel to $\{110\}$, with the same orientation as one of the pit walls (Fig. 6d).

A foil was also cut from the surface of an olivine grain fragment with a continuous Fe-Mg silicate coating and TEM images show that the coating is 1.2-1.6 μm thick (Fig. 7a). The olivine grain surface beneath lies parallel to (001) overall, but has very fine-scale (001) - $\{111\}$ serrations (Fig. 7a). The host grain contains dislocations that are visible in the bright-field images by virtue of their associated strain contrast (Fig. 7a, b). They are oriented parallel to $\{110\}$ so that they bisect the serrations, are spaced ~ 0.1 - $0.4\ \mu\text{m}$ apart when viewed along $[110]_{\text{ol}}$, and have a density of $\sim 4 \times 10^8\ \text{cm}^{-2}$ (Fig. 7a-c). There is an indistinct layering within the coating and the lower layer thickens to $\sim 0.5\ \mu\text{m}$ above depressions in the underlying olivine grain and thins to $\sim 0.2\ \mu\text{m}$ over its prominences (Fig. 7a). This Fe-Mg silicate is also very finely crystalline and yields a SAED pattern identical to that of the coating in Figure 6d. High-resolution images show that its constituent crystals are $< \sim 30\ \text{nm}$ in length by 2-4 lattice repeats in thickness, and their lattice plane spacings are ~ 1.10 - $1.35\ \text{nm}$ (Fig. 7d). The contact between olivine and the coating is very sharp, and in its

lowermost few tens of nanometres the constituent crystals of the coating are aligned with their long axes sub-parallel to the local olivine grain surface so that they ‘wrap around’ the serrations.

One of the coatings examined in plan view is compositionally zoned (Fig. 8). This coating overlies the surface of an olivine grain fragment containing aligned rectangular inclusions of augite, as highlighted in the Ca K_{α} X-ray map (Fig. 8). The coating has two compositionally distinct parts, namely a relatively Si-rich region and a 0.1 mm diameter disc-shaped area that is distinguished from the Si-rich region by its depletion with respect to Si and enrichment in Cl, Ca, Mn and Fe (Fig. 8). The Si-rich region of the coating is sufficiently thin (probably sub-micrometre) that augite inclusions beneath it are readily identifiable in the Ca K_{α} X-ray map (Fig. 8). The edges of the disc have broken during sample preparation to expose underlying layers, one of which is depleted in Si and enriched in C relative to the majority of the disc (Fig. 8, spectrum 4). The disc surface shows three concentric zones, an inner one that is rich in Ca and Mn, a middle zone that is rich in Cl, Si and Fe and the outer zone is again rich in Ca (Fig. 8). A small region on the left hand edge of the disc has relatively high concentrations of Na and Cl, which suggests that a halite grain is present just beneath the surface.

The Fe-Mg silicate coatings are sometimes intergrown with and cross-cut by a more coarsely crystalline Fe-Mg silicate (Fig. 9a). Qualitative X-ray microanalysis shows that it is compositionally very similar to the coating apart from having slightly high concentrations of C, Cl and Fe and lower concentrations of Si. Where it occurs as veins this second generation postdates fractures that cross-cut the coating (Fig. 9a). Examination of the broken interior of the second generation of Fe-Mg silicate shows that it is composed of very fine fibres, and contains micrometre sized crystals of Ca sulphate whose habit is suggestive of gypsum (Fig. 9b).

DISCUSSION

Development of secondary mineral veins

The interaction of liquid water with Nakhla is recorded by the veins that are seen in cross-section within the polished samples. The olivine grain fragments provide an additional and new perspective on secondary mineralisation because their Fe-Mg silicate coatings are interpreted to be selvages of the vein-filling Fe-Mg silicates that remained adhering to pieces of olivine grains after they had broken apart. The presence and thickness of the coatings is therefore determined by how the parent olivine grain fragmented during sample preparation. Fracturing along the axis of a vein would have produced two olivine grain fragments each with a relatively thin coating, but breakage of the parent olivine grain along the vein wall would have left one fragment with a thick coating whereas it would be absent from the counterpart fragment. In most cases the line of breakage was irregular so that olivine grain fragments have patchy coatings of variable thickness.

Creation of pore space

Velbel (2012) has outlined three mechanisms by which secondary mineral veins in nakhlite meteorites may have formed, which are summarised as follows: (i) cementation of intragranular fracture pores, with the first minerals to form crystallizing on the vein walls, (ii) cementation of intragranular pores formed by dissolution, again being filled from vein walls towards the vein axis, and (iii) isovolumetric replacement of the primary silicate, with the replacement front propagating from an initial fracture. The stratification of the different vein-filling minerals in Nakhla and the fine-scale layering and zoning of the Fe-Mg silicates is more consistent with an origin by pore filling than by replacement. This conclusion is consistent with the observation by Treiman and

Lindstrom (1997) that Fe-Mg silicate veins in Lafayette occur along the boundaries between grains of augite and plagioclase, and so cannot have formed solely by replacement of olivine. As regards the origin of pores that were present within olivine grains and along augite-olivine grain boundaries, there is good evidence that dissolution played a major role in their formation. This evidence includes the fact that symplectite lamellae cross-cut veins. Such a relationship is inexplicable if all of the veins formed from open fractures, but is consistent with an origin of the pore space by dissolution, with the symplectites dissolving substantially more slowly than olivine (dissolution rates of augite and olivine are discussed below). The other possibility that symplectites formed after the veins is highly unlikely given that the symplectites formed at such high temperatures that the hydrous Fe-Mg silicates would have recrystallized. Lamellar symplectites also occur together with secondary mineral veins in olivine from the Y-000593 nakhlite, and in common with Nakhla the symplectites may cross-cut the veins or project part way into them (Noguchi et al., 2009). The petrographic relationships of intergranular symplectites in Figure 2 can be explained by them having initially formed along an augite-olivine grain boundary, then the olivine being dissolved from around them to leave the symplectites in contact with augite and projecting into open pores.

The most compelling evidence for the formation of a pre-mineralisation porosity by dissolution is the microstructure of vein walls. The fine scale notches on serrated vein walls that are oriented close to $(001)_{ol}$ (Figs. 1–3 and 7a) are comparable in size and shape to the faceted etch pits that form in terrestrial olivine by laboratory dissolution (e.g. Wegner and Christie, 1976; Kirby and Wegner, 1978) and natural weathering (Banfield et al., 1990; Velbel, 2009a). Vein walls oriented parallel to $\sim(100)$ and $\sim(010)$ are also seen in plan view on the coating-free surfaces of olivine grain fragments and here they can contain regular lines of faceted pits that are again morphologically comparable to etch pits in terrestrial olivine (Velbel, 2009a). The three-dimensional shape of etch pits on (001) vein walls can be inferred from differences in their appearance with viewing direction (Fig. 10). The serrations are seen most clearly where (001) vein walls meet a surface near (100) , be it the polished surface of a thin section (Figs. 1–3) or FIB-produced foil (Fig. 4). Etch pits are however apparently absent where (001) vein walls intersect (010) parallel surfaces (Fig. 3b). Thus the long axes of the teeth and notches must extend parallel to (010) (i.e. the $[100]$ direction) so that in plan view vein walls oriented parallel to (001) have a corrugated texture (Fig. 10). As drawn in Figure 10 the etch pits have a $\{0kl\}$ form, but as those in Figure 7c have a $\{111\}$ profile the pits are more likely to be lenticular in shape with $\{hkl\}$ walls.

The humps on grain fragment coatings are interpreted to be Fe-Mg silicate casts of etch pits that were present on the piece of olivine that was removed during sample preparation (i.e. the opposite vein wall). The TEM image of a foil cut through one of these casts shows that a mirror image pit is present within olivine beneath (Fig. 6d), thus confirming that etch pits formed on both walls of the vein as would be expected if their location and shape were crystallographically controlled. Regarding the grain fragment in Figure 5, these bowl-shaped etch pits have developed on vein walls oriented near (100) ; their scarcity in the olivine grain fragments and thin sections studied must be because few veins have formed in that orientation. As the vein filling secondary minerals are demonstrably Martian in origin (Gooding et al., 1991), these etch pits must also have been produced by the action of water on Mars. Etch pits have also been described from olivine in the Miller Range [MIL] 03346 nakhlite. Velbel (2008, 2009b) and Velbel et al. (2010) interpreted them to have formed by terrestrial weathering because they occur only within a few hundred micrometres of the meteorite's outer surface and are free of preterrestrial secondary minerals. However Hallis and Taylor (2011) described 'conical etch pits' within its olivine grains that were

filled with Martian secondary minerals, and so in the case of MIL 03346 it is likely that the etch pits have formed both pre- and post-terrestrially.

Duration of mineral dissolution

The duration of dissolution required to form the pores that were subsequently mineralised to make veins can be estimated by calculating the rate of retreat (Rr) of a planar vein wall ($\mu\text{m yr}^{-1}$) using Equation 1:

$$Rr = (D \times V) \times 3.15 \times 10^{11} \quad (1)$$

where D is the dissolution rate of a mineral at a given condition ($\text{moles cm}^{-2} \text{s}^{-1}$) and V is its molecular volume ($\text{cm}^3 \text{mole}^{-1}$).

Values of D for augite and olivine vary with solution temperature (T) and pH (dissolution rates are also a function of solution chemistry, but this variable is not considered in the following calculations). As laihunite is absent from Nakhla olivine, in contrast to the Yamato nakhlites, fluid T s must have been $< \sim 400\text{--}800^\circ\text{C}$ (Noguchi et al., 2009). Treiman et al. (1993) suggested that the Lafayette secondary minerals crystallised at $< 100^\circ\text{C}$ and Changela and Bridges (2011) concluded that during at least part of its lifetime the nakhlite aqueous system had a T of $< 150^\circ\text{C}$ and a neutral to weakly acidic pH. Hallis and Taylor (2011) further suggested that the mineralizing solutions had a pH of 3.5–5.0. In the calculations of Rr we therefore assume that the solutions had a pH of 5, a T of 5°C , 25°C or 100°C , and were in contact with a perfectly planar vein wall for the entire duration of dissolution. Values for D of Nakhla olivine (i.e. Fa_{67}) have been determined using information in Stopar et al. (2006). These calculations yield values for Rr of between 8.01×10^{-2} and $5.05 \times 10^2 \mu\text{m yr}^{-1}$ (Table 3). Assuming that a $5 \mu\text{m}$ wide intragranular pore in olivine formed by removal of $2.5 \mu\text{m}$ from each wall, the values for Rr listed in Table 3 show that at pH 5/ 100°C the pore could have formed in 1.8 days and at pH 5/ 25°C the duration of etching increases to 3.1 yrs. These values are consistent with lifetimes for olivine particles on the surface of Mars calculated by Stopar et al. (2006). For example, they determined that a $2000 \mu\text{m}$ diameter grain of Fa_{35} olivine that was continuously in contact with pH 5/ 100°C solutions would dissolve completely in as little as 3 yrs.

As the widest veins in olivine are oriented close to $(001)_{\text{ol}}$, dissolution rates of Nakhla olivine grains clearly varied with the crystallographic orientation of the mineral surface in contact with aqueous solutions. The outcome of this orientation-selective etching is especially noticeable in Figure 2 where an intergranular vein ‘pinches out’ as the olivine wall rotates from near (001) to (010) . In order to make a $(001)_{\text{ol}}$ parallel pore it is necessary for solutions to firstly access the olivine grain along $(001)_{\text{ol}}$ (i.e. in the $[100]\text{--}[010]$ plane, Fig. 10), and then to etch the $(001)_{\text{ol}}$ parallel walls (i.e. dissolution parallel to $[001]$). Thus the dissolution rate of Nakhla olivine must have been greatest parallel to $[001]_{\text{ol}}$, although the fine-scale serrations of the vein walls show that they did not form by recession of a planar (001) surface but rather by enlargement and coalescence of $\{hkl\}$ notches. These findings are consistent with Banfield et al. (1990) and Welch and Banfield (2002) who showed that (001) parallel etch channels are commonplace in naturally weathered terrestrial fayalite, and this orientation selectivity reflects the preferential protonation of M1 octahedral cations. By contrast Awad et al. (2000) undertook experiments on terrestrial olivine (Fo_{91}) and found that grain surfaces retreated fastest parallel to $[010]$. The difference between results from Awad et al. (2000) and findings from the present study are likely to reflect contrasts in olivine microstructure as described below. Preferential dissolution of Nakhla olivine along $[001]$

cannot however account for why the veins are elongate in the [100]-[010] plane. An explanation is that the olivine grains contained hairline fractures, and those fractures that could be accessed by the aqueous solutions and whose walls were oriented close to (001)_{ol} were preferentially widened by etching parallel to [001]_{ol}. The origin of these fractures is also discussed below.

Data for augite D are unavailable over the same pH and T range as for olivine, but using values for pH 4.8/25 °C in Brantley and Chen (1995), the Rr for an augite surface is $5.04 \times 10^{-3} \mu\text{m yr}^{-1}$ (Table 3). This is only 0.6% of the Rr of an olivine surface under the same conditions (Table 2). Such a large difference in Rr accounts for why olivine was dissolved from around the symplectites to leave them projecting into open pores (Figs. 2 and 4) and why the secondary mineral veins within augite are much narrower than olivine (Fig. 2). Even where there is evidence for etching of augite vein walls to give the microdenticular textures that are a signature of terrestrial pyroxene weathering (Velbel and Losiak, 2010; Velbel, 2012), the amount of dissolution is far less than for olivine just a few micrometres away that is very likely to have been in contact with the same solutions (Fig. 2). In contrast to olivine therefore the mineralised pore space within augite is interpreted to have formed predominantly by fracturing and was widened very little by subsequent dissolution.

Timing of dissolution relative to shock

The most likely origin for the pre-dissolution fractures in augite and olivine is impact shock, and this is consistent with other microstructural evidence that Nakhla has experienced peak pressures of 14-20 GPa (Fritz et al., 2005). From results of $^{40}\text{Ar}/^{39}\text{Ar}$ step-heating of Nakhla augite, Cassata et al. (2010) showed that it had been briefly but intensely heated at 913 ± 9 Ma, which may constrain the timing of this shock event. Langenhorst et al. (1995, 1999) found that naturally and experimentally shocked olivine characteristically contains planar fractures in the low index orientations (100), (010), (001), (130) and (110), and observations from Nakhla in the present study suggest that the walls of those fractures (and grain boundaries) that were parallel or at a low angle to (001)_{ol} were selectively etched. Changela and Bridges (2011) have suggested that the nakhlite veins developed solely from shock, but the veins in Lafayette olivine grains are considerably wider than those in Nakhla ($\sim 15 \mu\text{m}$ vs $\sim 6 \mu\text{m}$, Changela and Bridges, 2011), despite Lafayette having experienced lower peak pressures (5-14 GPa, Fritz et al. 2005). The contrasts in vein width between Lafayette and Nakhla must therefore be due to processes in other than shock, for example a greater intensity of aqueous alteration.

The defects within olivine grains that occur on (100) and {110} (Figs. 3b, 6d and 7a) are further evidence for shock because comparable microstructures have been observed in naturally and experimentally shocked olivine (Ashworth and Barber, 1975; Langenhorst et al., 1995; Langenhorst et al., 1999). These defects were interpreted to be screw dislocations with a Burgers vector of [001] in the (100) and {110} glide planes and this agrees very well with orientations determined from Nakhla olivines (Fig. 10). The density of dislocations in Nakhla olivines ($\sim 2\text{--}4 \times 10^8 \text{ cm}^{-2}$) is similar to the density of dislocations in olivine from the Olivenza (LL5) meteorite ($10^8\text{--}10^9 \text{ cm}^{-2}$, Ashworth and Barber, 1975), which has experienced comparable shock pressures (i.e. shock stage S3, 15-20 GPa). By contrast, olivine in the Tenham (L6) meteorite has been shocked to 25-45 GPa and has a correspondingly greater dislocation density of $2 \times 10^{10} \text{ cm}^{-2}$ (Langenhorst et al., 1995). The laser shock experiments by Langenhorst et al. (1999) demonstrated that [001] screw dislocations develop in olivine simultaneously with the planar fractures, and that the density of both microstructures decrease with distance beneath the outer surface of the grain where pressures were greatest. Using

their experimentally determined relationship between fracture and dislocation density, the density of dislocations in Nakhla olivine ($\sim 2\text{--}4 \times 10^8 \text{ cm}^{-2}$) should correspond to ~ 20 fractures mm^{-2} , which is of the same order as the abundance of veins observed in the present study (e.g. Fig. 1).

If these planar fractures provided conduits for aqueous solutions to gain access to olivine grain interiors, the elastic strain associated with screw dislocations that formed in association with the fractures may have contributed to the crystallographic control on dissolution of fracture walls. This hypothesis is supported by the following observations: (i) the dislocation glide plane is parallel to the bases of etch pits on $\sim(100)$ olivine grain surfaces (Fig. 6d) and bisects $\{111\}$ etch pits on (001) parallel vein walls (Fig. 7a, c), and (ii) dissolution rates of Nakhla olivine grains were most rapid parallel to [001], which is the Burgers vector of the screw dislocations, and Kirby and Wegner (1978) experimentally demonstrated that etch pits can form where [001] screw dislocations meet (001) olivine grain surfaces. Thus, the simultaneous development of planar fractures and [001](100)/[001]{110} dislocations during shock can explain how aqueous solutions accessed grain interiors and also the strong crystallographic control on subsequent olivine dissolution. This hypothesis needs to be tested by microstructural work on olivine in other nakhlites and by dissolution experiments using naturally and experimentally shocked olivine.

Secondary mineralisation

Having established that etching created much of the pore space within Nakhla olivines that was occluded by carbonates and/or silicates, the relative timescales of dissolution and mineralisation can be assessed. These two processes may have taken place simultaneously or sequentially within the same aqueous system, or etching and mineralisation could have been discrete events mediated by aqueous solutions of a different composition and provenance.

As described below, the stratigraphy and cross-cutting relationships of the secondary minerals indicates that they were formed in the sequence of siderite, Fe-Mg silicate, a second generation of fibrous Fe-Mg silicate then gypsum. This carbonate-silicate-sulphate sequence is consistent with previous observations of nakhlite alteration products (Bridges and Grady, 2000; Changela and Bridges, 2011), but the new findings in the present study provide additional insights into fluid composition and availability.

Carbonate crystallization

Where siderite and the Fe-Mg silicate are juxtaposed the carbonate is always earlier, indicating that the first mineralizing solutions were HCO_3^- rich and reducing. As the olivine etch pits are free of Fe oxides/oxyhydroxides, dissolution must have also been mediated by reducing solutions, and so there is evidence for a qualitative continuity of fluid Eh between pore formation and the first phase of pore filling. Despite crystallizing in fluid-filled pores, siderite is absent from augite, and where veins occur along augite-olivine grain boundaries siderite is present only on the olivine wall (Fig. 2). This apparent preference of siderite for olivine substrates suggests that interaction of the HCO_3^- rich solutions with olivine was an important driver of carbonate mineralisation. It is therefore possible that siderite has formed by replacement of olivine, and Velbel (2012) has also suggested that Nakhla olivine could have been corroded during carbonate precipitation to leave etch pits.

Fe-Mg silicates

The ease by which the Fe-Mg silicate coatings separate from olivine to leave clean etch pits or perfect casts of them shows that the bond between the Fe-Mg silicate and olivine is very weak. As discussed earlier, this finding is consistent with formation of most of the Fe-Mg silicate by cementation rather than by topotactic replacement whereby some continuity between the crystal structures of olivine and its alteration products may be expected. Nonetheless there is some evidence for replacement of olivine where it projects into the vein interior, and this replacive Fe-Mg silicate has a more open texture (Fig. 3d). The sub-micrometre scale stratification of the Fe-Mg silicate as seen in cross-section (Fig. 7a) and in profile (Figs. 6c and 8) indicates that it was deposited as sheets on vein walls, and in at least one case the Fe-Mg silicate sheet formed by radial growth outwards from a nucleus to produce a disc (Fig. 8). Therefore solution chemistry must have varied significantly between deposition of individual sheets to give them their different compositions (compare spectra 1 and 4 in Fig. 8), and also fluctuated during formation of sheets to produce the prominent compositional zoning (Fig. 8). Thus the Fe-Mg silicate must have formed slowly in comparison to the rate of change of the composition of ambient solutions, and their chemistry may have fluctuated in response to introduction of solutions of different compositions by flow. If the solutions were static, their chemistry may have changed in response to temporal variations in the proportions of different primary minerals undergoing dissolution, or by withdrawal of solutes as minerals crystallized elsewhere.

Despite the abundance within nakhlites of Fe-Mg silicates whose chemical composition is consistent with a Fe-rich smectite (Gooding et al., 1991), or Fe-smectite plus some serpentine (Changela and Bridges, 2011), their mineralogy is controversial. From TEM images of ion milled Nakhla foils Ashworth and Hutchison (1975) stated that “the fine-grained alteration products become colloidal towards the centre of the vein”. By TEM characterisation of foils made using ultramicrotome Gooding et al. (1991) concluded that the Fe-Mg silicates are “generally poorly crystalline” although they contain crystallites typically a few nanometres in size, but up to 15 nm, with 1.1-1.5 nm lattice fringe spacings. Hydrous silicates are more varied in Lafayette but Treiman et al. (1993) described vein fills most similar to those in Nakhla (the constituents of their ‘fine-grained intragranular veinlets’) that have a <20 nm crystal size and are composed of smectite with a 1 nm lattice plane spacing. Noguchi et al. (2009) found that vein-filling silicates in the Y-000593 and Y-000749 nakhlites are nanocrystalline (~3-4 lattice repeats in thickness) and in two areas of the sample the crystallites were found to have lattice spacings of ~0.74 and ~1.04 nm, consistent with serpentine and saponite respectively, and 0.97-1.06 nm, again suggestive of smectite. Most recently Changela and Bridges (2011) have concluded from TEM characterisation of foils cut from nakhlite olivine grains using the FIB technique that the Fe-Mg silicate is an amorphous gel. Results from all of the foils examined by TEM in the present study show that the Fe-Mg silicates are crystalline and their 1.10-1.35 nm basal layer spacings are consistent with a collapsed smectite. These results are therefore in agreement with the findings of Gooding et al. (1991), Treiman et al. (1993) and Noguchi et al. (2009) that the very finely crystalline Fe-Mg silicate vein fills are predominantly nanocrystalline smectite.

Treiman and Lindstrom (1997) suggested that the secondary minerals in Lafayette had been initially deposited as a ‘gel’ and from the same solutions that had congruently dissolved olivine or mesostasis glass; the abundance of Al in veins cross-cutting mesostasis in comparison to veins within olivine is good evidence for localised provenance of the solutes. However they also proposed that this ‘gel’ then crystallised to produce the hydrous silicate minerals now observed (Treiman et al., 1993). The very fine crystal size of the nanocrystalline smectite in Nakhla is unusual in

comparison to the coarser phyllosilicates that characterise terrestrial serpentinised olivine (e.g. Plümper et al., 2012), but is comparable to phyllosilicates described from the Y-791198 CM carbonaceous chondrite by Chizmadia and Brearley (2008). These phyllosilicates are 2-5 lattice repeats in thickness and are inferred to have formed by crystallisation of an amorphous precursor that had been prevented from coarsening further by the low T after initial crystallisation, probably coupled with a scarcity of aqueous solutions. Such water-limited coarsening of the smectite is also consistent with late-stage evaporation of the nakhlite aqueous system hypothesised by Changela and Bridges (2011). The model is supported further by the characteristic fracturing of the nanocrystalline smectite coatings on olivine grain fragments found in the present study (Fig. 9a), which is reminiscent of desiccation cracks that develop by drying of fine-grained terrestrial sediments.

The hypothesis of rapid water loss is however called into question by the observation that nanocrystalline smectite is intergrown with and cross-cut by a second and more coarsely crystalline generation of Fe-Mg silicate, itself encrusted by gypsum. This later Fe-Mg silicate could not be unambiguously identified, although the presence of very fine fibres (Fig. 9b) is suggestive of a phyllosilicate, and from its qualitative chemical composition it is probably a serpentine. This identification is reasonable because phyllosilicates are commonplace in Lafayette (Treiman et al., 1993; Changela and Bridges, 2011). As serpentine veins cross-cut fractures within the nanocrystalline smectite (Fig. 9b), this second episode of silicate mineralisation must have postdated desiccation. Taken together, these findings suggest that after deposition of the smectite aqueous solutions withdrew from Nakhla, or parts of it. Subsequently solutions rich in Mg, Si and Fe returned to crystallise the serpentine but for a sufficiently brief time that the smectite was not fully rehydrated.

Sulphates

As microcrystalline gypsum is intimately intergrown with serpentine its precise position in the mineralisation sequence is difficult to determine, and a post-terrestrial origin cannot be excluded. However previous studies have concluded that gypsum crystallized from the last vestiges of the Martian water (Bridges and Grady, 2000; Changela and Bridges, 2011), and observations in the present study are consistent with these findings.

Model for fluid evolution in Nakhla

The primary reason for the greater abundance and diversity of secondary minerals within olivine than augite is that under the ambient conditions olivine dissolved at a much greater rate than augite and so developed a higher porosity and permeability. The preference of siderite for olivine rather than augite substrates implies that continuing liberation of solutes from the vein walls was a driver for mineralisation (i.e. by dissolution-reprecipitation or replacement), and once HCO_3^- was exhausted, Mg, Si and Fe derived from the olivine contributed to crystallisation of smectite. This phase of mineralization was followed by the crystallization of small volumes of Fe-Mg phyllosilicate and gypsum. Although it is possible that secondary mineralization was terminated owing to water loss by desiccation (or freezing), there may have just been very little pore space remaining so that fluids could not gain access to grain interiors.

The evidence from Nakhla suggests that solutions were more or less static and that dissolution and mineralisation were near-simultaneous on an intragranular scale. This scenario is consistent with the previous nakhlite alteration models of Treiman et al. (1993) and Treiman and

Lindstrom (1997), which were based on analyses of Lafayette. They suggested that most of the cations required to form secondary minerals (principally Mg, Al, Si, Ca, Mn and Fe), were derived from within the nakhlite lithology in a low water/rock system. Specifically they calculated that the minerals could have formed by reaction of water with 45-65% olivine plus 35-55% mesostasis glass with only Cl, S and P being imported from beyond the parent rock. If etching and mineralisation were essentially simultaneous, Nakhla must have remained free of aqueous solutions capable of etching olivine for ~280 Ma between shock fracturing at ~913 Ma and secondary mineralisation at ~633 Ma.

CONCLUSIONS

The crystallisation of secondary minerals from aqueous solutions at shallow depths in the Martian crust was facilitated by a period of dissolution, which was probably very brief, and olivine was affected to a much greater extent than augite. The aqueous solutions exploited pre-existing fractures, possibly shock-formed, and selectively widened and extended those within olivine whose walls were oriented close to (001). Dissolution was most rapid along [001], probably due to the presence of [001](100) and [001]{110} dislocations that formed simultaneously with the planar fractures. In addition to increasing intra- and inter-crystalline porosity and permeability, dissolution of the olivine grains supplied many of the cations required for the siderite, nanocrystalline smectite and phyllosilicate. The carbonate-silicate-sulphate mineralisation sequence observed is consistent with a short lived aqueous system, although its evolution was not as straightforward as a progressive loss of water through evaporation or freezing because Fe-Mg phyllosilicate and gypsum crystallized after desiccation fracturing of the nanocrystalline smectite. If the ~913 Ma thermal event recorded by Nakhla augite was synchronous with shock deformation of the rock, then ~280 Ma elapsed between opening of the fractures and aqueous activity, thus highlighting the scarcity of crustal water during the Amazonian epoch.

Acknowledgements

We thank Billy Smith and Colin How (School of Physics & Astronomy, University of Glasgow) for their help with the FIB and TEM respectively, Peter Chung (School of Geographical and Earth Sciences, University of Glasgow) for assistance with the SEM work and Chris Hayward (University of Edinburgh) for help with the EPMA. We are also grateful to John Bridges (University of Leicester) for valuable discussions of nakhlite aqueous alteration, and to Mike Velbel, Alex Ruzicka and an anonymous reviewer for helpful and informative comments on the manuscript. This work was funded by the UK Science and Technology Facilities Council.

REFERENCES

- Ashworth J. R. and Barber D. J. 1975. Electron petrography of shock-deformed olivine in stony meteorites. *Earth and Planetary Science Letters* 27:43–50.
- Ashworth J. R. and Hutchison R. 1975. Water in non-carbonaceous stony meteorites. *Nature* 256:714–715.
- Awad A., Koster van Groos A. F. and Guggenheim S. 2000. Forsteritic olivine: effect of crystallographic direction on dissolution kinetics. *Geochimica et Cosmochimica Acta* 64:1765–1772.
- Banfield J. F., Veblen D. R. and Jones B. F. 1990. Transmission electron microscopy of subsolidus oxidation and weathering of olivine. *Contributions to Mineralogy and Petrology* 106:110–123.
- Borg L. and Drake M. J. 2005. A review of meteorite evidence for the timing of magmatism and of surface or near-surface liquid water on Mars. *Journal of Geophysical Research* 110:E12S03.
- Boudier F., Baronnet A., and Mainprice D. 2010. Serpentine mineral replacements of natural olivine and their seismic implications: oceanic lizardite versus subduction-related antigorite. *Journal of Petrology* 51:495–512.
- Brantley S. L. and Chen Y. 1995. Chemical weathering rates of pyroxenes and amphiboles. In *Chemical weathering rates of silicate minerals*, edited by White A. F. and Brantley S. L. Reviews in mineralogy, vol. 31. Washington D.C.: Mineralogical Society of America. pp. 119–172.
- Bridges J.C. and Grady M.M. 2000. Evaporite mineral assemblages in the nakhlite (martian) meteorites. *Earth and Planetary Science Letters* 176:267–279.
- Bridges J. C. and Warren P. H. 2006. The SNC meteorites: Basaltic igneous processes on Mars. *Journal of the Geological Society, London* 163:229–251.
- Bridges J. C., Catling D. C., Saxton J. M., Swindle T. D., Lyon I. C., and Grady M. M. 2001. Alteration assemblages in the Martian meteorites: Implications for near-surface processes. In *Chronology and evolution of Mars*, edited by Kallenbach R., Geiss J., and Hartmann W. K. Kluwer: Dordrecht. pp. 365–392.
- Cassata W. S., Shuster D. L., Renne P. R., and Weiss B. P. 2010. Evidence for shock heating and constraints on Martian surface temperatures revealed by $^{40}\text{Ar}/^{39}\text{Ar}$ thermochronometry of Martian meteorites. *Geochimica et Cosmochimica Acta* 74:6900–6920.
- Changela H. G. and Bridges J. C. 2011. Alteration assemblages in the nakhlites: Variation with depth on Mars. *Meteoritics & Planetary Science* 45:1847–1867.
- Chizmadia L. J. and Brearley A. J. 2008. Mineralogy, aqueous alteration, and primitive textural characteristics of fine-grained rims in the Y-791198 CM2 carbonaceous chondrite: TEM observations and comparison to ALH81002. *Geochimica et Cosmochimica Acta* 72:602–625.
- Eugster O., Busemann H., Lorenzetti S., and Terrebilini D. 2002. Ejection ages from krypton-81-krypton-83 dating and pre-atmospheric sizes of martian meteorites. *Meteoritics & Planetary Science* 37:1345–1360.
- Friedman-Lentz R. C., Taylor G. J. and Treiman A. H. 1999. Formation of a martian pyroxenite: a comparative study of the nakhlite meteorites and Theo's Flow. *Meteoritics & Planetary Science* 34:919–932.
- Fritz J., Artemieva N., and Greshake A. 2005. Ejection of Martian meteorites. *Meteoritics & Planetary Science* 40:1393–1411.
- Gooding J. L., Wentworth S. J., and Zolensky M. E. 1991. Aqueous alteration of the Nakhla meteorite. *Meteoritics* 26:135–143.
- Grady M. M., Anand M., Gilmour M. A., Watson J. S., and Wright I. P. 2007. Alteration of the Nakhlite lava pile: Was water on the surface, seeping down, or at depth, percolating up? Evidence (such as it is) from Carbonates (abstract #1826). 38th Lunar and Planetary Science Conference. CD-ROM.

- Hallis L. and Taylor G. J. 2011. Comparisons of the four Miller Range nakhlites, MIL 03346, 090030, 090032 and 090136: Textural and compositional observations of primary and secondary mineral assemblages. *Meteoritics & Planetary Science* 46:1787–1803.
- Harvey R. P. and McSween H. Y. Jr 1992. Petrogenesis of the nakhlite meteorites: Evidence from cumulate mineral zoning. *Geochimica et Cosmochimica Acta* 56:1655–1663.
- Kirby S. H. and Wegner M. W. 1978. Dislocation substructure of mantle-derived olivine as revealed by selective chemical etching and transmission electron microscopy. *Physics and Chemistry of Minerals* 3:309–330.
- Korochantseva E. K., Schwenzer S. P., Buikin A. I., Hoppe J., Ott U., and Trierloff M. 2011. ^{40}Ar - ^{39}Ar and cosmic-ray exposure ages of nakhlites–Nakhla, Lafayette, Governador Valadares–and Chassigny. *Meteoritics & Planetary Science* 46:1397–1417.
- Langenhorst F., Joreau P., and Doukhan J. C. 1995. Thermal and shock metamorphism of the Tenham chondrite: A TEM examination. *Geochimica et Cosmochimica Acta* 59:1835–1845.
- Langenhorst F., Boustie M., Migault A., and Romain J. P. 1999. Laser shock experiments with nanosecond pulses: a new tool for the reproduction of shock defects in olivine. *Earth and Planetary Science Letters* 173:333–342.
- Lee M. R., Bland P. A., and Graham G. 2003. Preparation of TEM samples by focused ion beam (FIB) techniques: applications to the study of clays and phyllosilicates in meteorites. *Mineralogical Magazine* 67:581–592.
- Lee M. R. and Smith C. L. 2006. Scanning transmission electron microscopy using a SEM: applications to mineralogy and petrology. *Mineralogical Magazine* 70: 561–572.
- Lentz R. C. F. McCoy T. J. Taylor G. J. 2005. Multiple Nakhlite lava flows? *Meteoritics & Planetary Science* 40:A91.
- Mikouchi T., Yamada I., and Miyamoto M. 2000. Symplectic exsolution in olivine from the Nakhla martian meteorite. *Meteoritics & Planetary Science* 35:937–942.
- Mikouchi T., Koizumi E., Monkawa A., Ueda Y., and Miyamoto M. 2003. Mineralogical comparison of Y000593 with other nakhlites: Implications for relative burial depths of nakhlites (abstract #1944). 34th Lunar and Planetary Science Conference. CD-ROM.
- Mikouchi T., Miyamoto M., Koizumi E., Makishima J., and McKay G. 2006. Relative burial depths of nakhlites: An update (abstract #1865). 37th Lunar and Planetary Science Conference. CD-ROM.
- Mikouchi T., Makishima J., Kurihara T., Hoffmann V. H., and Miyamoto M. 2012. Relative burial depth of nakhlites revisited (abstract #2363). 43rd Lunar and Planetary Science Conference. CD-ROM.
- Needham A. W., Abel R. L., Tomkinson T., Johnson D., and Grady M. M. 2011. Pooling of water and the formation of evaporite minerals in the Martian subsurface (abstract #2148). 42nd Lunar and Planetary Science Conference. CD-ROM.
- Noguchi T., Nakamura T., Misawa K., Imae N., Aoki T., and Toh S. 2009. Laihunite and jarosite in the Yamato 00 nakhlites: Alteration products on Mars? *Journal of Geophysical Research* 114:E10004.
- Plümper O., King H.E., Vollmer C., Ramasse Q., Jung H. and Austrheim H. 2012. The legacy of crystal-plastic deformation in olivine: high-diffusivity pathways during serpentinisation. *Contributions to Mineralogy and Petrology* 163:701–724.
- Rao M. N., Sutton S. R., McKay D. S., and Dreibus G. 2005. Clues to Martian brines based on halogens in salts from nakhlites and MER samples. *Journal of Geophysical Research* 110:12.
- Sawyer D. J., McGhee M. D., Canepa J., and Moore C. P. 2000. Water soluble ions in the Nakhla martian meteorite. *Meteoritics & Planetary Science* 35:743–747.
- Shirai N. and Ebihara M. 2008. Chemical characteristics of Nakhlites: Implications to the geological setting for Nakhlites (abstract #1643). 39th Lunar and Planetary Science Conference. CD-ROM.

- Stopar J. D., Taylor G. J., Hamilton V. E., and Browning L. 2006. Kinetic model of olivine dissolution and extent of aqueous alteration on Mars. *Geochimica et Cosmochimica Acta* 70:6136–6152.
- Treiman A. H., Barrett R. A., Gooding J. L. 1993. Preterrestrial aqueous alteration of the Lafayette (SNC) meteorite. *Meteoritics* 28:86–97.
- Treiman A. H. and Lindstrom D. J. 1997. Trace element geochemistry of Martian iddingsite in the Lafayette meteorite. *Journal of Geophysical Research* 102:9153–9163.
- Treiman A. H. 2005. The nakhlite meteorites: Augite-rich igneous rocks from Mars. *Chemie der Erde* 65:203–270.
- Velbel M. A. 2008. Aqueous corrosion textures of olivine in Mars meteorite MIL03346 (abstract #1905). 39th Lunar and Planetary Science Conference. CD-ROM.
- Velbel M. A. 2009a. Dissolution of olivine during natural weathering. *Geochimica et Cosmochimica Acta* 73:6098–6113.
- Velbel M. A. 2009b. Corrosion textures formed by aqueous alteration of Mars meteorite olivine and terrestrial analogs (abstract #4036). *Workshop on Modelling Martian Hydrous Environments*.
- Velbel M. A. 2012. Aqueous alteration in Martian meteorites: Comparing mineral relations in igneous-rock weathering of Martian meteorites and in the sedimentary cycle of Mars. In *Sedimentary Geology of Mars*, edited by Grotzinger J. and Milliken, R. Society for Sedimentary Geology Special Publication, p. 97-117.
- Velbel M. A., Stopar, J. D., Taylor, G. J., and Vicenzi E. P. 2010. Aqueous alteration of olivine in Mars meteorite MIL03346: Corrosion textures and redistribution of elements in alteration products (abstract #2223). 41st Lunar and Planetary Science Conference. CD-ROM.
- Velbel M. A. and Losiak A. I. 2010. Denticles on chain silicate grain surfaces and their utility as indicators of weathering conditions on Earth and Mars. *Journal of Sedimentary Research* 80:771-780.
- Welch S. A., and Banfield J. F. 2002. Modification of olivine surface morphology and reactivity by microbial activity during chemical weathering. *Geochimica et Cosmochimica Acta* 66:213–221.
- Wegner M. W. and Christie J. M. 1976. Chemical etching of dislocations in forsterite. *Contributions to Mineralogy and Petrology* 59:131–140.
- Wogelius R. A. and Walther J. V. 1992. Olivine dissolution kinetics at near-surface conditions. *Chemical Geology* 97:101-112.

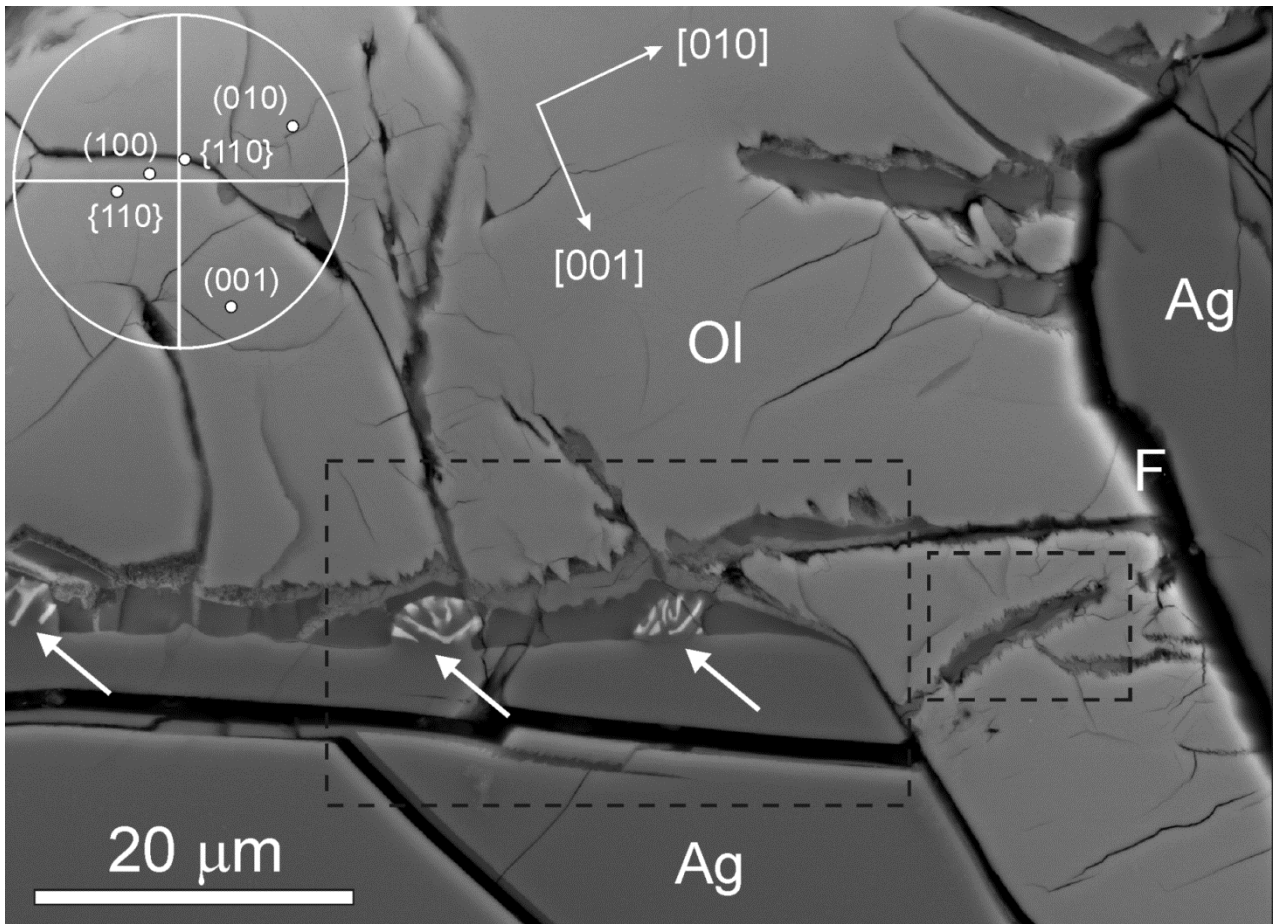


Fig. 1. BSE image of an olivine (Ol) grain in polished thin section. The olivine is in contact with an augite grain (Ag, bottom) and contains an augite inclusion (Ag, upper right). An EBSD pole figure showing the orientations of low order olivine planes is inset. The polished olivine surface lies at 17° to (100). Olivine is cut by veins containing siderite (medium grey) and Fe-Mg silicate (dark grey). The widest veins within olivine are oriented parallel or at a low angle to the trace of $(001)_{ol}$ and their walls are finely serrated. The wall of the open fracture between the olivine grain and augite inclusion (F) is oriented close to $(010)_{ol}$ and where veins meet this fracture it can be seen that they lie at a high angle to the polished grain surface and so their true orientation is close to $(001)_{ol}$. Narrower veins are elongate parallel to $(010)_{ol}$. Hairline fractures project part way across the olivine grain and they are oriented parallel to the trace of $(001)_{ol}$. The vein between olivine and the augite grain encloses three hemispherical augite-magnetite symplectites (arrowed) and its olivine wall is finely serrated. A trench was cut through this vein and images of its $(010)_{ol}$ face reveal that the olivine vein wall lies at a high angle to the polished surface so that its true orientation is close to $(001)_{ol}$.

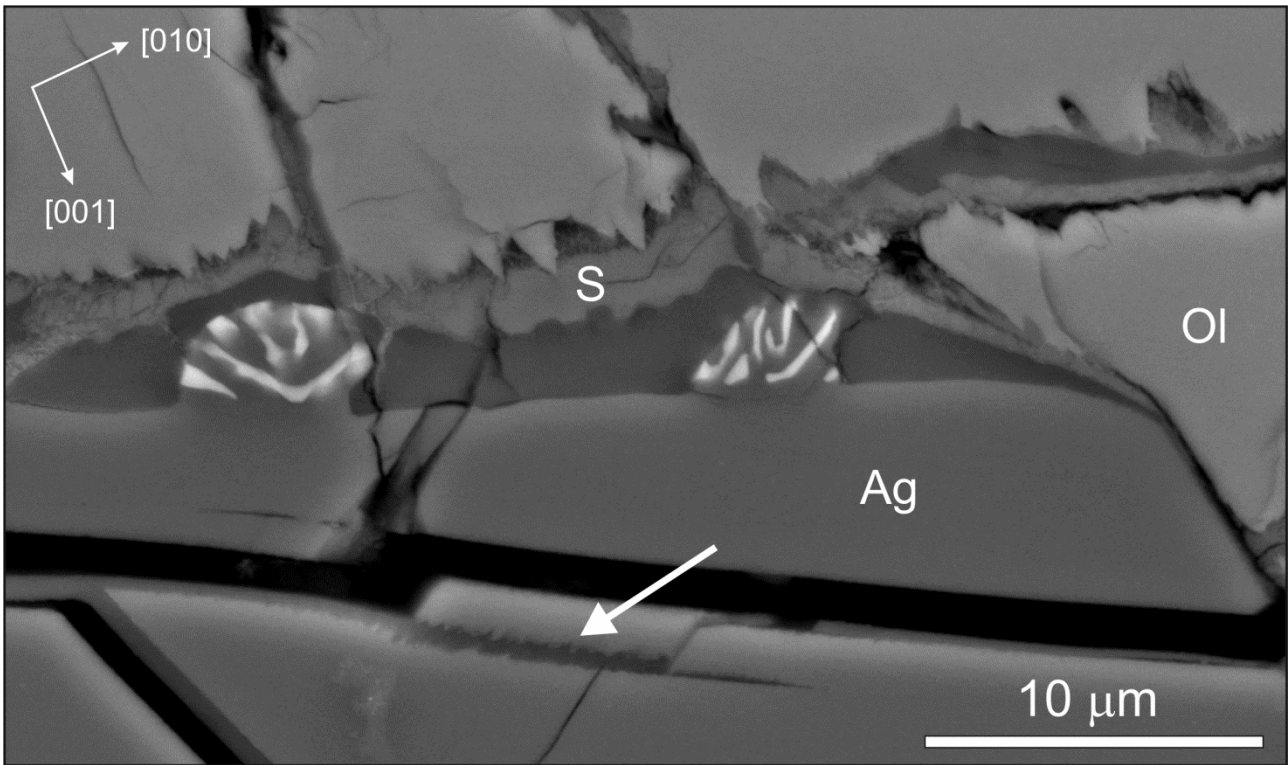


Fig. 2. BSE image of the intergranular vein in the left hand side rectangle of Figure 1. Teeth and notches on the serrated (001) olivine (Ol) vein wall are elongate parallel to [001] and in this two-dimensional view have a $\{0kl\}$ form where $k > 4l$. The olivine is lined by siderite (S) whereas the augite vein wall is in contact with Fe-Mg silicate. This vein narrows abruptly towards the right hand side of this image as the augite-olivine grain boundary rotates from near $(001)_{ol}$ to parallel to the trace of $(010)_{ol}$. Fe-Mg silicate veins occur within augite (Ag) and the walls of some of these veins have very fine serrations ('microdenticles', arrowed). Fe-Mg silicate coats only one side of the open fractures, indicating that they opened along vein walls at some time after secondary mineralisation.

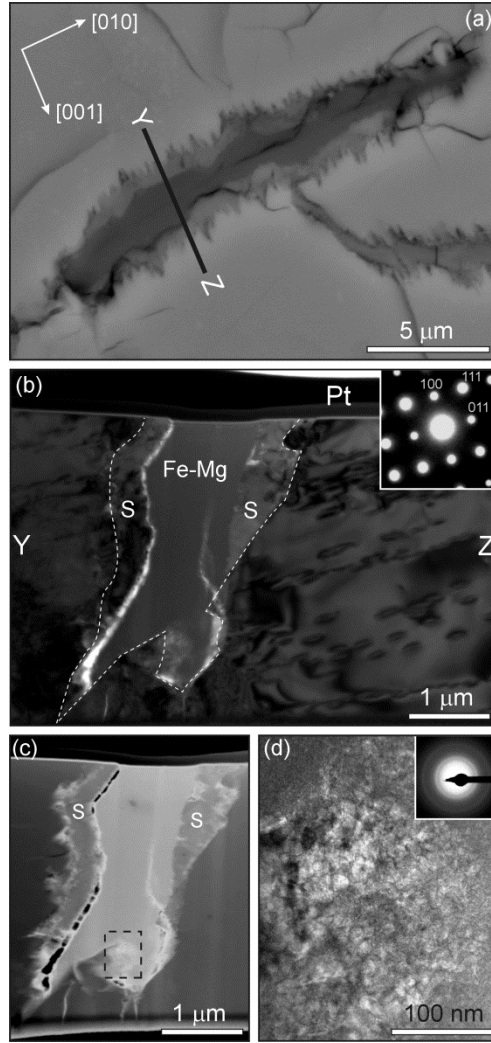


Fig. 3. Images of an intragranular vein in the right hand side rectangle in Figure 1. (a) BSE image showing that the finely serrated vein walls are lined by siderite (mid-grey) with Fe-Mg silicate (dark grey) along the vein axis. Teeth and notches of the serrations are elongate parallel to [001]. (b) Bright-field TEM image of a foil cut along the line Y-Z in (a), with the $[0\bar{1}1]$ SAED pattern inset. The midplane of the foil is close to $(010)_{ol}$. The vein lies at a high angle to the polished surface and so as the EBSD pole figure in Figure 1 shows, its axis lies close to $(001)_{ol}$. SAED reveals that olivine on either side of the vein differs in orientation by $\sim 5^\circ$, and so the vein has developed along a low angle subgrain boundary. The olivine contains linear defects that are oriented parallel to the trace of (100). The olivine vein wall is delineated by a dashed white line and is planar or irregular with some sections oriented parallel to the trace of $\{111\}$. Siderite (S) is between olivine and the axial Fe-Mg silicate (Fe-Mg). (c) Dark-field LV-STEM image of part of the foil. The olivine, siderite (S) and Fe-Mg silicate are clearly distinguished by differences in their scattering intensity, and this image reveals that the bottom of the vein is close to the base of the foil, although veinlets extend further into the olivine. (d) Bright-field TEM image of the contact between olivine and Fe-Mg silicate at the base of the vein (the boxed area in (c)), with a SAED pattern inset. This contact is very irregular, as seen in (c), and the Fe-Mg silicate has an open structure with circular crystallites. The SAED pattern shows that the Fe-Mg silicate is very finely crystalline and its two rings have d-spacings of 0.261 nm and 0.157 nm.

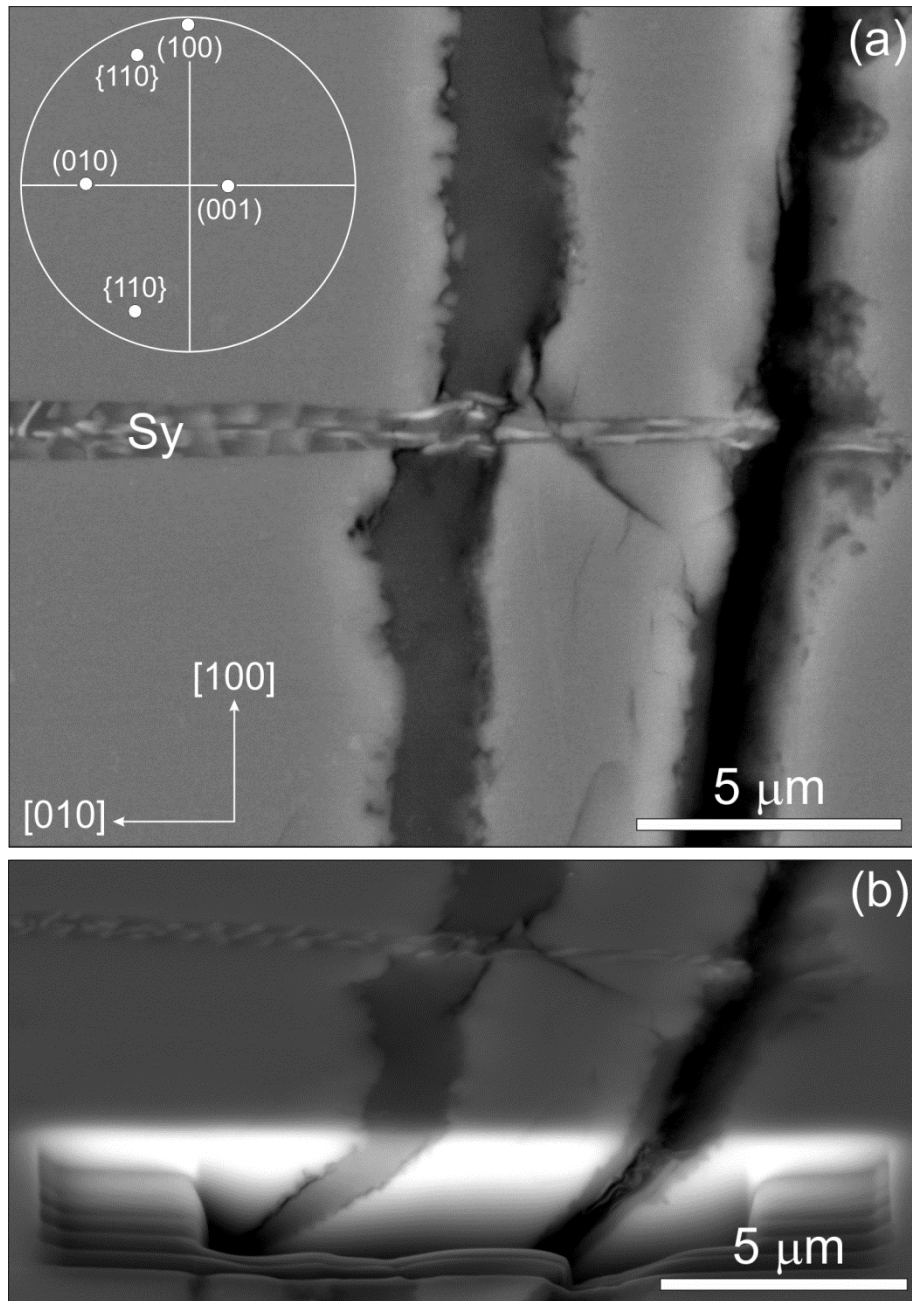


Fig. 4. (a) BSE image of the interior of an olivine grain. The inset EBSD pole figure shows that the polished surface of this grain lies at $\sim 90^\circ$ to the polished surface of the olivine grain in Figures 1–3. This grain contains a narrow parallel sided Fe-Mg silicate vein and an open fracture. The vein and fracture intersect a symplectite lamella (Sy) containing an intergrowth of magnetite (white) with augite (mid-grey). This lamella cross-cuts the Fe-Mg silicate vein, albeit with some distortion, and is itself cut and slightly offset by the open fracture. (b) BSE image of the area in (a) following cutting of a trench using the FIB technique. The thin section has been tilted by 60° so that the (100) face of the trench can be studied, and this image shows that the vein and fracture are parallel to each other and oriented close to $(010)_{ol}$. This image also reveals that the fracture is lined by Fe-Mg silicate. The white band in the upper part of the trench is a charging artefact.

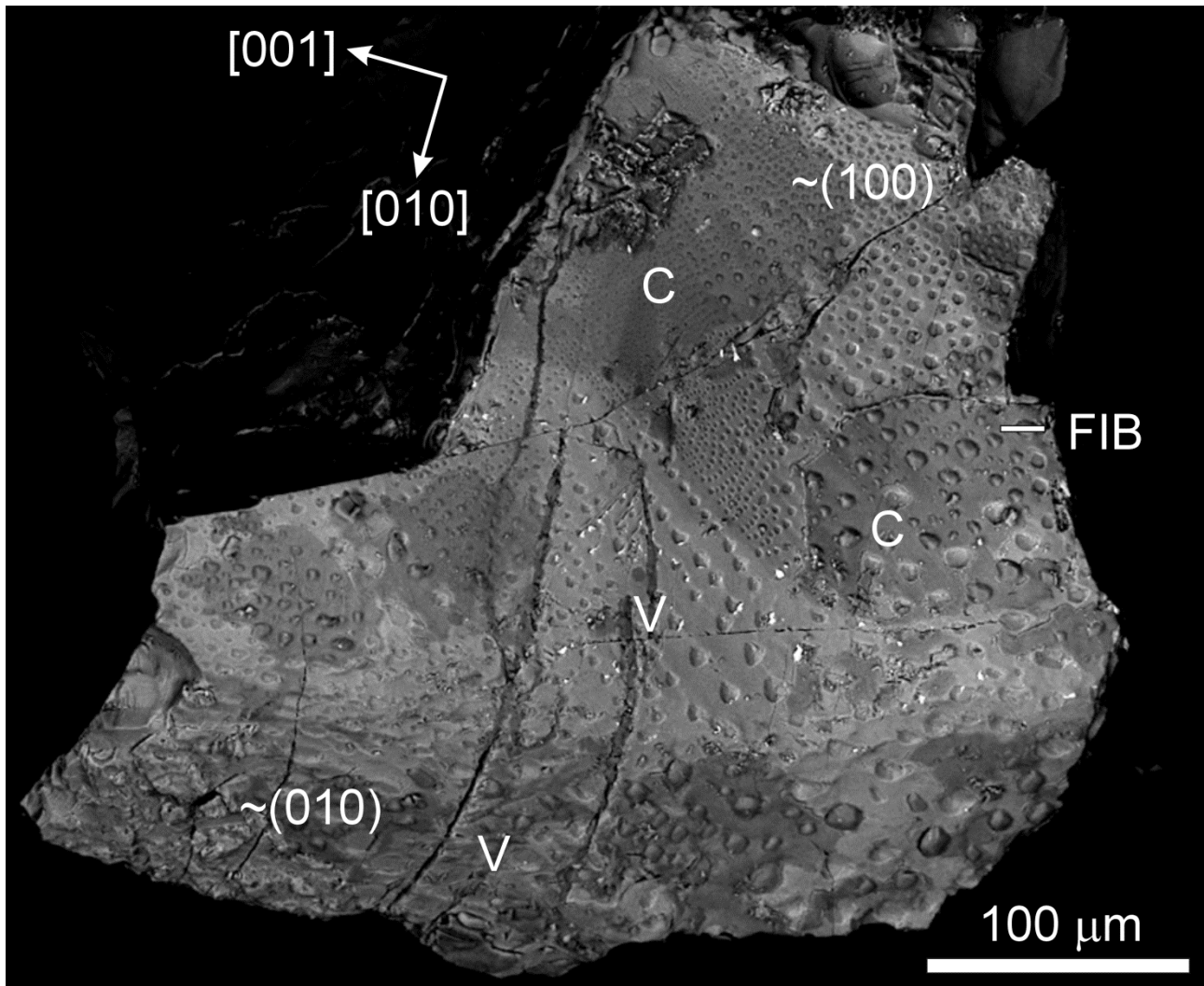


Fig. 5. BSE image of an olivine grain fragment with the approximate crystallographic orientations of its surfaces indicated. The dark grey lines in the lower left of the grain that are aligned approximately parallel to $[010]_{\text{ol}}$ are veins of secondary minerals (V). Where the olivine grain surface is exposed (light grey) it contains parallel lines of pits. Other parts of the grain surface have a coating with a lower mean atomic number than the olivine (C, medium grey), and this coating has regularly spaced humps of similar size, shape and alignment to the pits in olivine. The short white line next to 'FIB' marks the midplane of a foil extracted from the coating and olivine beneath.

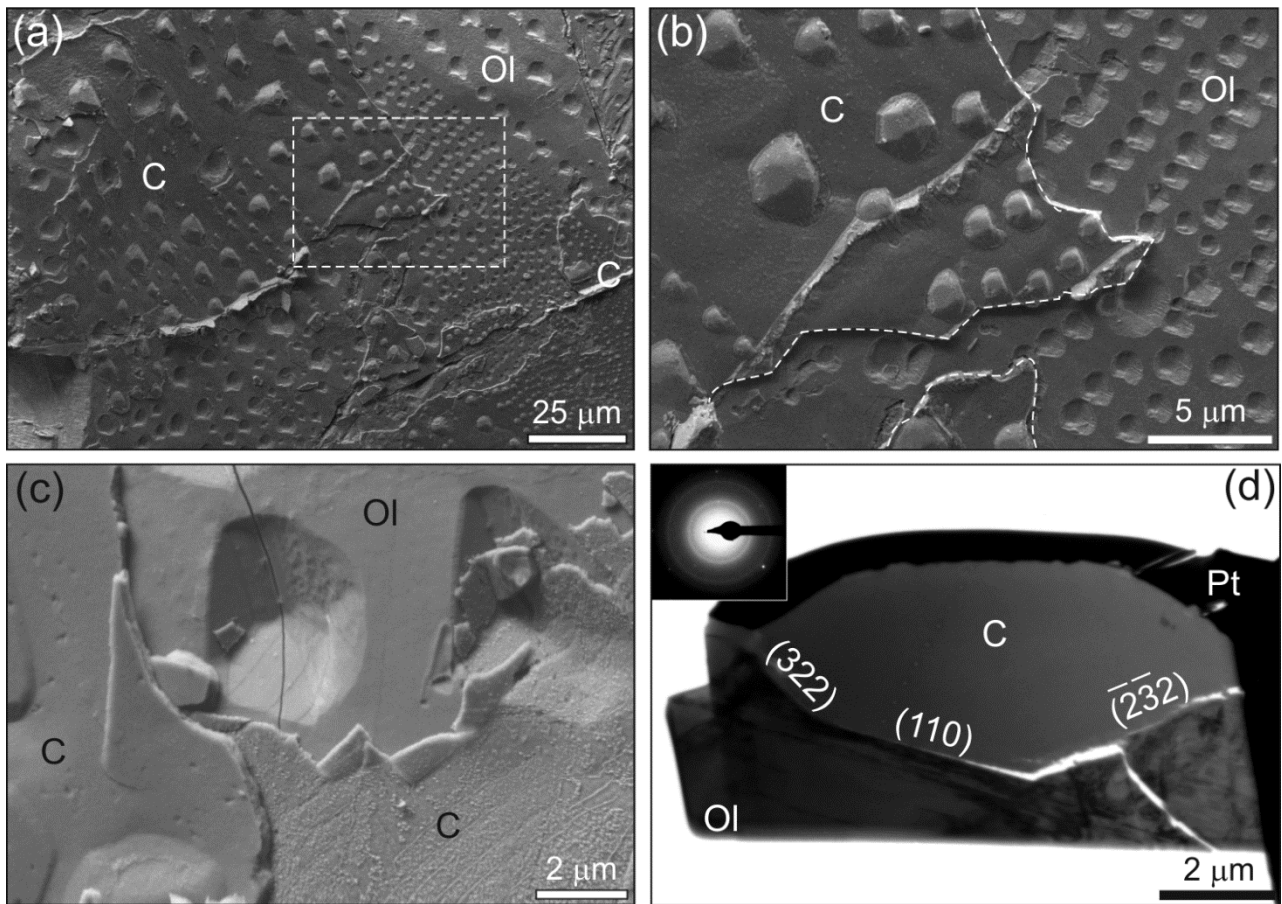


Fig. 6. Images from the $\sim(100)$ surface of the olivine grain fragment in Figure 5. (a) SE image showing that the Fe-Mg silicate coating (C) has lines of regularly spaced humps whereas the olivine (Ol) has pits that are also arranged in parallel lines. (b) SE image of the boxed part of (a) illustrating the faceted and asymmetric shapes of the pits in olivine (Ol) and the humps on the coating (C). The dashed white line delineates the broken edge of the coating. (c) SE image of the coating (C) and olivine (Ol) beneath. The coating has broken to expose two layers. The lower and thinner layer (lower right) has a nanoscale ornamentation and lines the pit walls whereas the upper and thicker layer (left) has a smooth outer surface with humps. (d) Bright-field TEM image of a foil cut through a hump (see Figure 5 for location). The platinum strap (Pt) has been deposited over its rounded top. In the olivine beneath is a pit whose margins are crystallographically controlled and their orientations as determined from a $[\bar{2}21]$ SAED pattern are indicated. The olivine (Ol) contains lamellar microstructures that lie parallel to the (110) etch pit base. A SAED pattern acquired from the coating is inset.

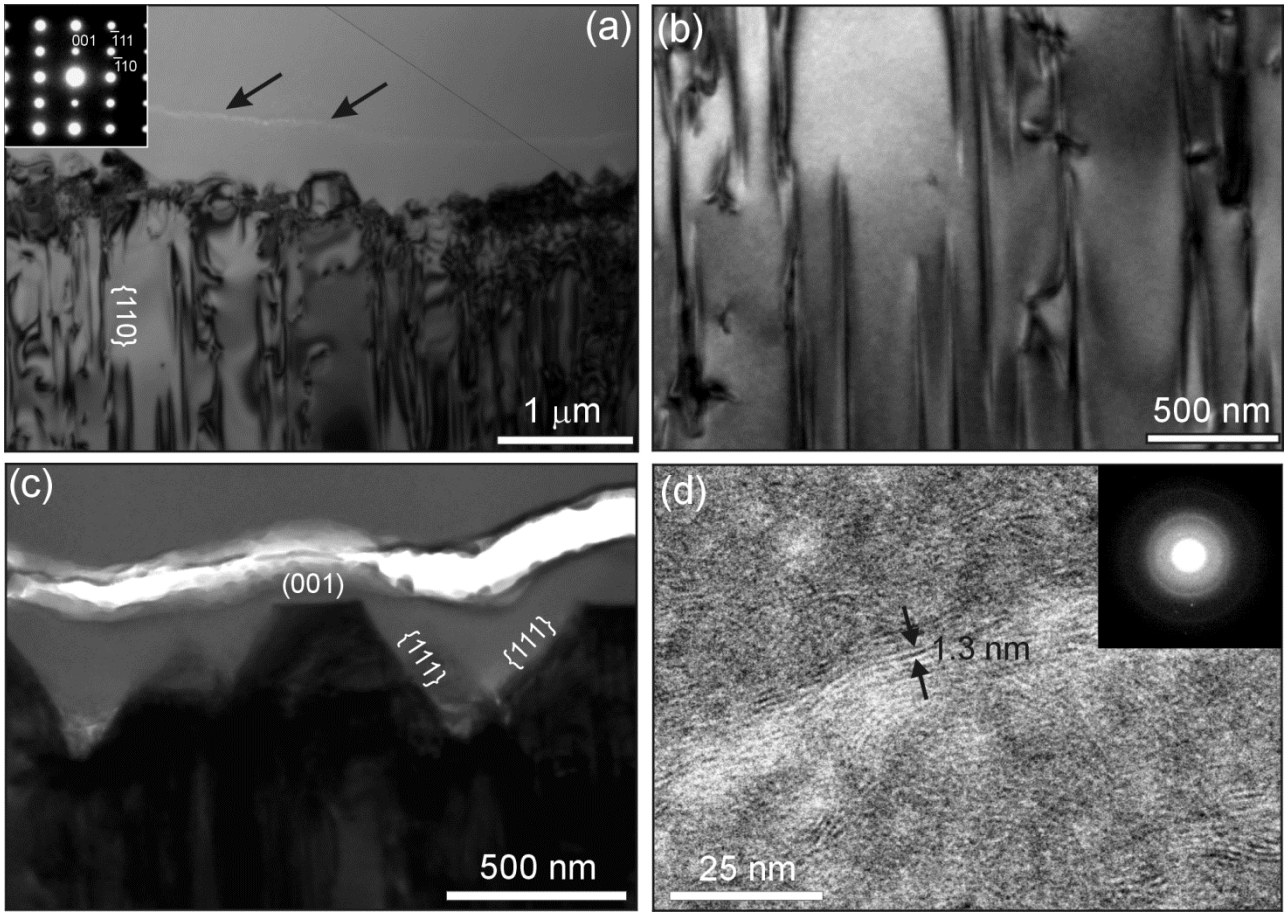


Fig. 7. TEM images of a foil cut from the (001) parallel surface of a coated olivine grain fragment. (a) Bright-field image showing the olivine grain (lower half of the image) and coating (upper half). The olivine grain contains {110} parallel defects, that are identified as screw dislocations, and its surface is serrated on the sub-micrometre scale. A faint line (arrowed) separates two layers of the coating. The [110] SAED pattern from the olivine is inset. (b) Bright-field image of the interior of the olivine grain in (a) and with the foil in the same orientation. The {110} parallel dislocations are highlighted by strain contrast. (c) Bright-field image of the olivine-coating interface with the olivine in the same crystallographic orientation as (a) and (b). The profile of the serrations is defined by (001)_{ol} and {111}_{ol} planes. The white band within the coating is a fracture that has formed during sample preparation. (d) High-resolution image of the coating with corresponding SAED pattern inset. The image shows that the coating is very finely crystalline and this is confirmed by the continuous rings in the SAED pattern that have d-spacings of 0.257 nm and 0.157 nm. The constituent crystals are a couple of ~1.3 nm lattice repeats in thickness.

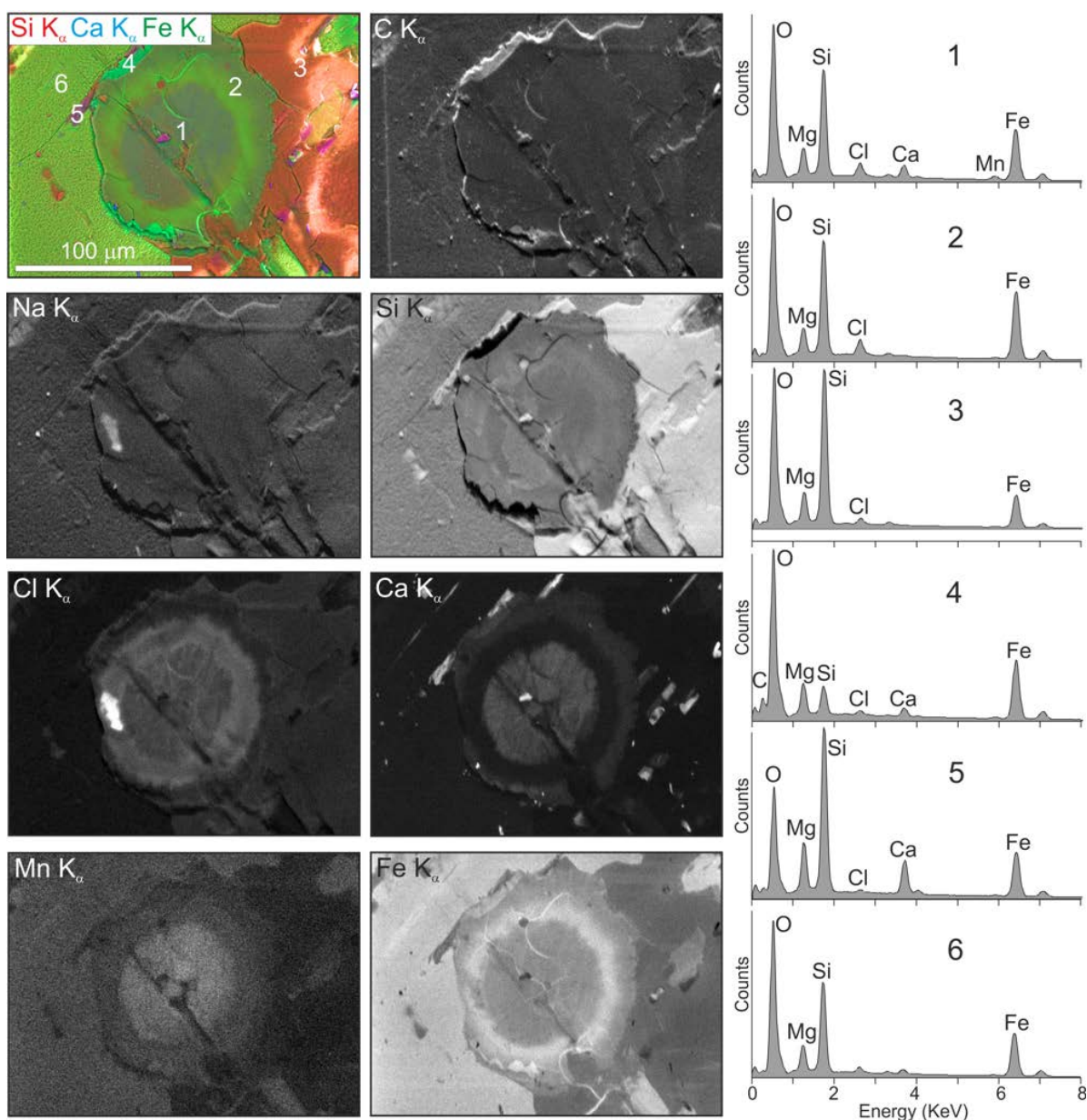


Fig. 8. X-ray maps and spectra of a Fe-Mg silicate coating on an olivine grain fragment. In the top left is a multi-element map overlain on a SE image. The six numbered points mark the sites from where X-ray spectra were extracted from $5 \times 5 \mu\text{m}$ sized areas of the original 1024×768 pixel spectrum map. Spectra 1 and 2 are from the zoned Fe-Mg silicate disc, 3 is from Fe-Mg silicate surrounding the disc, 4 is from a lower layer of the coating that has been exposed by fracturing (note the C peak), 5 is from an augite inclusion within olivine and 6 is from the olivine grain. As both the augite and olivine spectra show a small Cl peak it is likely that they have a very thin Fe-Mg silicate coating.

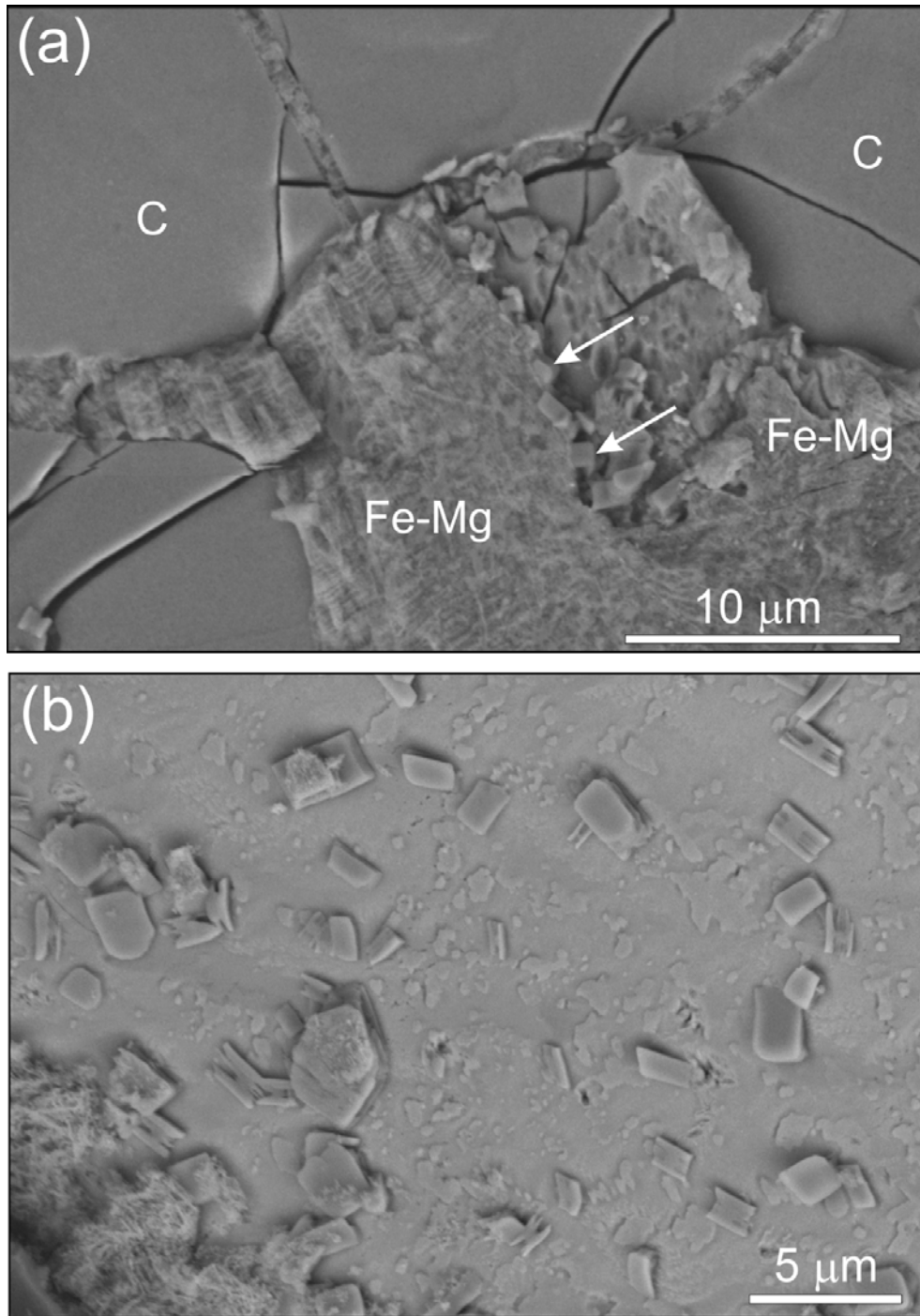


Fig. 9. Images of the coated surface of an olivine grain fragment. (a) SE image showing a Fe-Mg silicate coating (C) that is intergrown with a compositionally similar but more coarsely crystalline Fe-Mg silicate (Fe-Mg). Veins of the coarser Fe-Mg silicate cross-cut the coating and postdate fractures within it. Crystals of calcium sulphate, probably gypsum (arrowed), encrust one edge of the coarser Fe-Mg silicate. (b) BSE image of euhedral crystals of Ca sulphate, probably gypsum, that have been exposed by removal during sample preparation of the coarsely crystalline Fe-Mg silicate with which they were intergrown. Fibres of the Fe-Mg silicate encrust gypsum crystals in the lower left hand side of the image.

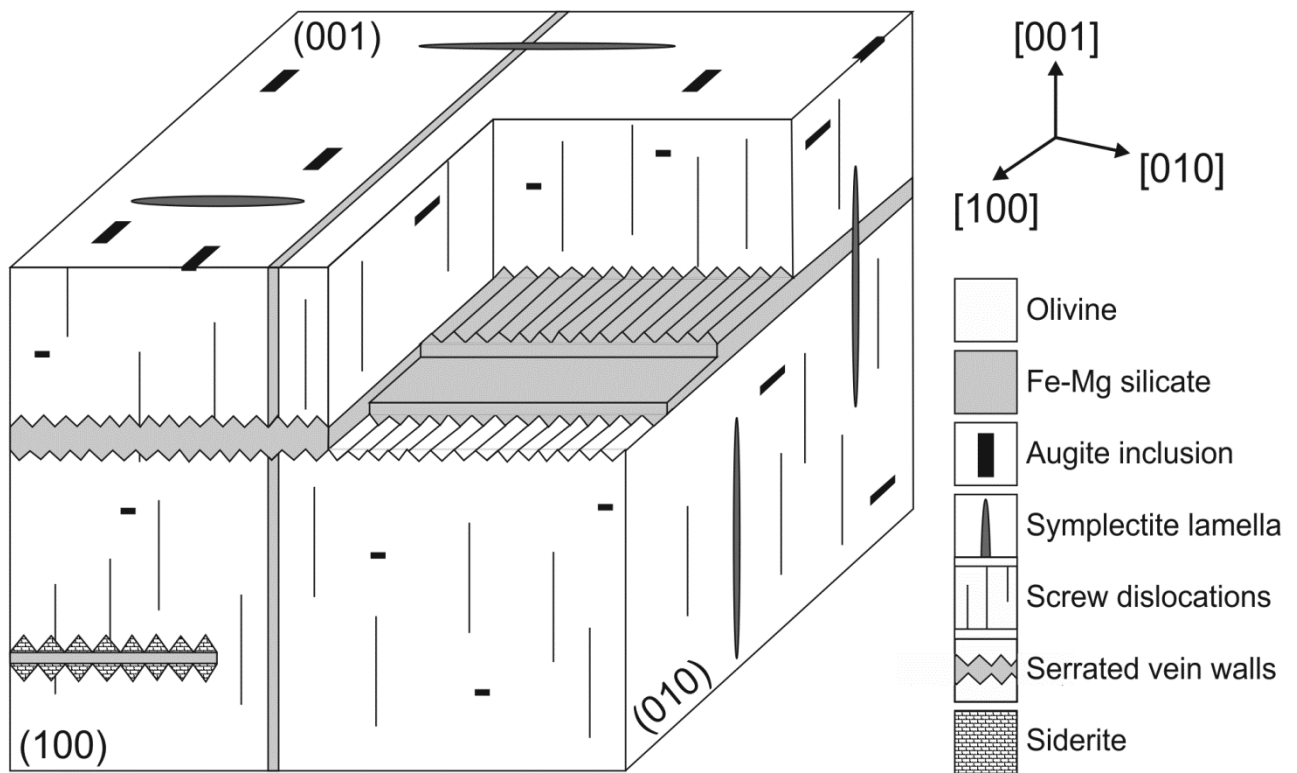


Fig. 10. Schematic diagram (not to scale) of a Nakhla olivine grain showing the orientation relationships of secondary mineral veins, etch pits, screw dislocations, lamellar symplectites and augite inclusions. Note that the etch pits as drawn have the form of $\{0kl\}$, but are more likely to be lenticular (i.e. discontinuous along $[100]$) and to have a $\{hkl\}$ form.

Table 1. Mean chemical compositions of Nakhla augite and olivine.

	Augite	Olivine
SiO ₂	50.51 (1.26)	32.72 (0.25)
TiO ₂	0.17 (0.11)	0.02 (0.01)
Al ₂ O ₃	0.70 (0.41)	dl
FeO	15.57 (2.33)	51.70 (0.52)
MnO	0.41 (0.05)	0.92 (0.04)
MgO	12.76 (1.70)	14.40 (0.40)
CaO	18.24 (0.16)	0.35 (0.07)
Na ₂ O	0.21 (0.04)	dl
Cr ₂ O ₃	0.35 (0.09)	dl
Total	98.92	100.10
n	4	7
	No. ions per 6 O	No. ions per 4 O
Si	1.954	0.997
Al	0.032	-----
Ti	0.005	0.000
Mg	0.735	0.654
Fe	0.505	1.317
Mn	0.013	0.024
Ca	0.756	0.012
Na	0.016	-----
Cr	0.011	-----
	Atomic percentages	
En	36.6	
Fs	25.8	
Wo	37.6	
Fa		66.8

Data obtained by EPMA and expressed as wt%. n denotes number of analyses and figures in parentheses are standard deviations. dl denotes below detection limits, and K and Ni were below detection limits in all analyses.

Table 2. Chemical compositions of vein-filling Fe-Mg silicates in Nakhla determined here and in previous studies.

	This study ^a	Gooding et al. (1991) ^b	Changela and Bridges (2011) ^c
SiO ₂	41.58 (4.09)	40.20	39.50
TiO ₂	0.02 (0.01)	0.02	0.02
Al ₂ O ₃	0.12 (0.24)	0.78	0.12
Cr ₂ O ₃	0.01 (0.01)	0.03	dl
FeO	31.03 (3.60)	34.25	34.50
MnO	0.61 (0.15)	0.63	0.79
NiO	dl -----	<.01	na
MgO	8.57 (1.01)	6.82	6.20
CaO	0.33 (0.49)	1.14	1.24
Na ₂ O	0.09 (0.17)	1.16	0.24
K ₂ O	0.31 (0.19)	0.60	0.49
SO ₃	0.11 (0.03)	0.14	0.05
Cl	1.20 (0.39)	0.66	0.25
P ₂ O ₅	0.01 (0.01)	0.06	na
Total	83.97	86.49	83.40
n	4	13	78

Results are expressed as wt% and are the mean (and standard deviation) of n analyses. Figures in parentheses are standard deviations. ^aData obtained by EPMA. ^bDescribed as ‘rust’. ^cDescribed as ‘gel’. dl denotes below detection limits and na denotes not analysed.

Table 3. Data for the calculation of retreat rates of augite and olivine vein walls.

	Augite ¹	Olivine ²	Olivine ²	Olivine ²
<i>T</i> and pH conditions	25 °C, pH 4.8	5 °C, pH 5	25 °C, pH 5	100 °C, pH 5
Dissolution rate (<i>D</i>) (mol cm ⁻² s ⁻¹)	2.50×10 ⁻¹⁶	5.60×10 ⁻¹⁵	5.61×10 ⁻¹⁴	3.53×10 ⁻¹¹
Molar volume (<i>V</i>) (cm ³ mol ⁻¹)	64.06	45.43	45.43	45.43
Retreat rate (<i>Rr</i>) (μm yr ⁻¹)	5.04×10 ⁻³	8.01×10 ⁻²	8.03×10 ⁻¹	5.05×10 ²

¹*D* for Wo₄₄En₅₁Fs₅ augite from Sverdrup (1990) in Brantley and Chen (1995). ²*D* for Fa₆₇ determined using data in Stopar et al. (2006). *Rr* is calculated using Equation 1.